magis

Propagation Losses Through Common Building Materials

2.4 GHz vs 5 GHz

Reflection and Transmission Losses Through Common Building Materials

Prepared by:
Robert Wilson[1]
Graduate Student
University of Southern California[2]

For:
James A. Crawford, CTO
Magis Networks, Inc.
August 2002

---

[1] robertwilson@ieee.org
[2] A special note of thanks to Robert Wilson who performed all of this work during the 2002 summer, and his advisor, Dr. Robert Scholtz, Director of the UltraLab at USC. A further note of thanks to Vulcan Ventures which donated USC's anechoic chamber that was used in conducting all of these measurements.

Abstract

Many recently published accounts that compare wireless local area network (WLAN) performance between 2.4 GHz and 5 GHz systems make many claims regarding higher propagation losses at 5 GHz as compared to 2.4 GHz. While it is true that Friis' formula dictates that propagation losses will be $20\text{Log}_{10}(5.25/2.4) \cong 6.8$ dB higher at 5 GHz in the case of isotropic transmit and receive antennas, propagation losses through most building and home-construction materials are almost the same for both frequency regimes.

An extensive materials-loss measurement program was recently conducted at the University of Southern California (USC) under contract with Magis Networks. The program investigated propagation loss using USC's large on-campus anechoic chamber. This report documents the measurement techniques used and the results obtained. Aside from large cement blocks and red bricks that displayed somewhat more loss at 5 GHz than at 2.4 GHz (Table 3), losses for all other materials tested were very much the same in both frequency regimes.

1. Measurement Goals

The experiment described in the following pages was performed to investigate RF propagation through different common building materials over a range of frequencies. More specifically, to make a comparison between the transmitted, reflected, and absorbed energy in two frequency bands, the 2.2 – 2.4 GHz ISM and the 5.15-5.35 GHz UNII bands. Both bands are specified for use in WLAN systems in the IEEE 802.11 standards.

2. Prior Work

Materials characterization experiments fall into two categories. The first category is tests performed on composite materials, either in-situ within buildings or custom built in the laboratory, with the purpose of determining and modeling losses through typical structures. These are consistently free-space tests, which are generally performed with standard gain horn antennas. Examples of materials tested in a laboratory setting are glass, limestone, and brick walls [1], concrete walls [2], and metal stud walls with gypsum board [3]. In-situ tests have been performed for building floors [4], as well as exterior [5] and interior [6,7] walls.

The second type of tests are those performed on homogenous materials, with the aim of determining the precise complex permittivity of the material, which can then be used in the calculation of the theoretical loss through any composite. A number of techniques have been developed, the most common determine complex permittivity from measured scattering parameters when the sample is placed in the path of an electromagnetic wave traveling in a waveguide, coaxial line [8,9], or free space [10,11,12,13,14,15]. The technique used to measure the RF energy varies depending on the type of material and frequency range under consideration. An overview of different techniques can be found in [16,17,18] and a comparison of techniques in [19].

3. EM Testing

Many models have been developed for waves propagating through structures and materials, both homogenous [8,9] and composite [2,3]. Sophisticated models for homogenous materials use internal multi-reflection models and can determine the relative permittivity of the material within a fraction of a percent [9], while models for composite materials take into account the optical grating effects of periodic structures such as concrete blocks with webs and voids, and interior walls with steel supporting studs [20]. A first order approach to permittivity estimation is taken here, using the dual assumptions of a planar incident wave and infinite plane-parallel dielectric material. Moreover, the permittivity is assumed to be constant over the observed frequency range. For composite structures an estimate of the effective relative permittivity of the composite is made, although the equations governing the behavior of waves in composite structures are more complex than for homogeneous material.

3.1 Electromagnetic Waves and Dielectric Materials

The solution to the wave equations for a transverse electromagnetic wave result in the following descriptions for the field components of an electromagnetic wave traveling in a homogenous medium of impedance Z at time t and at a point in space z [10],

$$E(t,z) = E_0 e^{-jwt+gz}$$
$$H(t,z) = H_0 e^{-jwt+gz} = \frac{E_0}{Z_1} e^{-jwt+gz} \qquad (1)$$

where $j = \sqrt{-1}$, $g = j\frac{w}{c}\sqrt{\tilde{m}_r \tilde{e}_r}$, $Z_1 = \sqrt{\frac{\tilde{m}_r m_0}{\tilde{e}_r e_0}}$, ω is the angular frequency of the wave, c is the speed of light, $\tilde{m}_r, \tilde{e}_r$ are the relative permeability and permittivity of the medium respectively, and m_0, e_0 are the dielectric constant and magnetic permeability of a vacuum.

For the remainder of this report we will assume the use of non-magnetic materials, i.e., $\tilde{m}_r = 1$, therefore the phase and attenuation of an electromagnetic wave passing through a homogenous dielectric material in free space are fully determined by their complex permittivity. The complex permittivity can be written as, $\tilde{e}_r = e_r(1 + j\frac{s}{we_0}) = e_r(1 + j\tan\partial)$ where σ is the conductivity of the material, and $\tan\partial$ is known as the loss tangent. If $s = 0$, then g is purely real and the wave undergoes only a phase shift and no attenuation as it passes through the material.

3.2 Scattering Parameters

Any two port system can be modeled by 4 complex scattering parameters, which are functions of the incident and reflected voltages at each port, refer to Figure 1.

$$R_0 = S_{11} = \frac{V_{r1}}{V_{s1}}$$
$$T_0 = S_{21} = \frac{V_{r2}}{V_{s1}}$$
$$S_{12} = \frac{V_{r1}}{V_{s2}} \qquad (2)$$
$$S_{22} = \frac{V_{r2}}{V_{s2}}$$

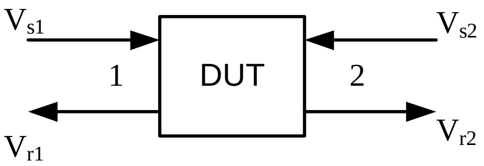

Figure 1: Two-Port Network

The Automatic Network Analyzer (ANA) measures these complex scattering parameters, giving the relationship between input and output electric fields, from which we can calculate directly the transmitted and reflected power of the network.

3.3 Determination of Relative Permittivity

For measuring the scattering parameters of a dielectric material in free space, we can use the equations in this section to calculate the relative permittivity of the material, assuming a planar incident wavefront and an infinite plane-parallel plate dielectric slab. Imposing boundary conditions at the interface of the dielectric material, that is, that the tangential components of the electric and magnetic fields must be continuous, we get a system of equations relating the transmission and reflection coefficients of the system, the electric fields, and the dielectric properties of the material. Referring to Figure 2, we have:

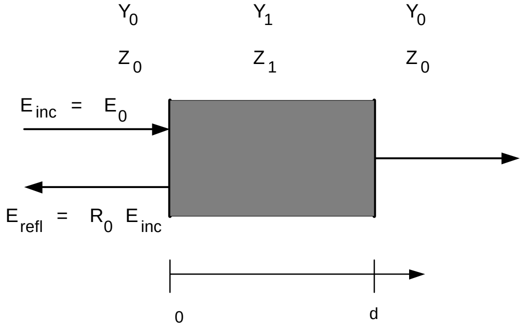

Figure 2: Electric Field Components for a Plane Electromagnetic Wave Incident on an Infinite Plane Dielectric Slab in Free-Space

$$\mathrm{E}_0(1 + \mathrm{R}_0) = \mathrm{E}_1(1 + \mathrm{R}_1)$$
$$\frac{\mathrm{E}_0}{\mathrm{Z}_0}(1 - R_0) = \frac{E_1}{Z_1}(1 - R_1)$$
$$E_1\left(e^{g_1 d} + R_1 e^{-g_1 d}\right) = T_0 E_0 \qquad (3)$$
$$\frac{E_1}{Z_1}\left(e^{g_1 d} - R_1 e^{-g_1 d}\right) = T_0 \frac{E_0}{Z_0}$$

where $g_i = j(2p / l_0)\sqrt{\tilde{e}_{ri}}$, $Z_i = \frac{g_0}{g_1} Z_0$, $\tilde{e}_{ri}$ is the complex relative permittivity of medium "i" and Z_i is the impedance of medium "i". The solutions in R_0 and T_0 for this system of equations are given by [10]:

$$R_0 = \frac{\left(g_0^{\ 2} - g_1^{\ 2}\right) e^{-g_1 d} - \left(g_0^{\ 2} - g_1^{\ 2}\right) e^{g_1 d}}{\left(g_0 + g_1\right)^2 e^{-g_1 d} - \left(g_0 - g_1\right)^2 e^{g_1 d}}$$

$$T_0 = \frac{4 g_0 g_1}{\left(g_0 + g_1\right)^2 e^{-g_1 d} - \left(g_0 - g_1\right)^2 e^{g_1 d}} \tag{4}$$

The power transmission and reflection coefficients are then given by

$$T = \left|T_0^2\right| \qquad R = \left|R_0\right|^2 \tag{5}$$

and $T + R + A = 1$, where A is the power coefficient of absorption.

4. Measurement Technique

All measurements were performed in the anechoic chamber facility at USC, eliminating interference from outside sources and minimizing multipath reflections. The antennas were a pair of ETS-Lindgren 3115 double-ridged guided horns, with stated bandwidth of 1-18 GHz. The test setup was similar to that used in [11], but scaled to suit the lower frequencies under consideration here. The setup consisted of an antenna in the "quiet zone" at each end of the chamber, 16 feet apart, with the sample holder 30 inches from the transmit antenna. The sample holder was a 4'x4' frame of signal absorbing material (SAM) facing the transmitter, with a 17"x17" square cut in the center, corresponding to 2.9 wavelengths at 2GHz. The SAM frame is designed to minimize diffraction around the sample. See Figure 3 for a schematic diagram of the set-up, and Figures 4, 5, and 6 for photographs.

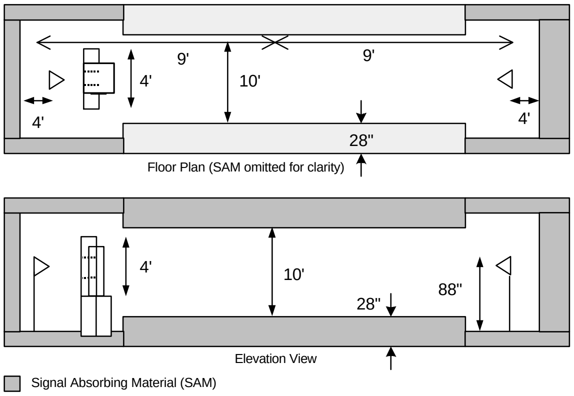

Figure 3: Measurement Setup

An HP8720D Network Analyzer (ANA) was used to measure the scattering parameters with each material in the sample window, with the transmit antenna connected to port 2, and the receive antenna to port 1. The ANA was set up to sweep from 1 – 12 GHz in 801 steps, using an IF bandwidth of 30 kHz, and averaging over 4 sweeps to reduce noise. The frequency range was restricted by the antenna gain at the low end and the capabilities of the feeding cables at the high end. In fact, in the analysis in the next section, only data up to 7GHz was deemed to be reliable. Calibration was performed at the connection points with the antennas, so the measured scattering parameters are those of the cascaded network of antennas and propagation path, where the propagation path might include any or all of: line-of-sight propagation through the material, diffraction at the outside edges of frame and inside edges of sample window, other multipath components reflected from the test rig, and other objects in the chamber.

Figure 4: Transmit Antenna, Absorbing Frame and Copper Reference Plate in Frame Window

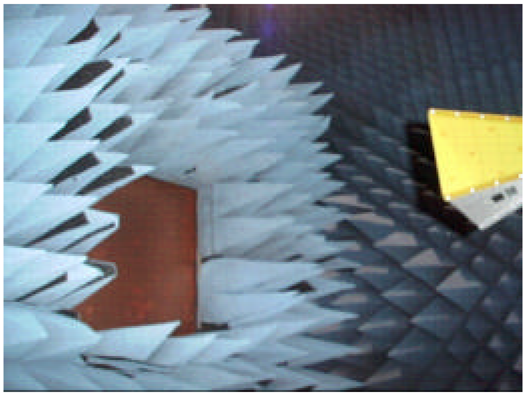

Figure 5: Test Rig and Receive Antenna

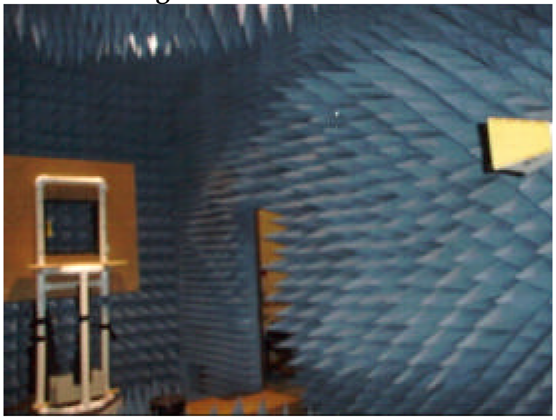

Figure 6: Sample Holder Test Rig and Transmit Antenna

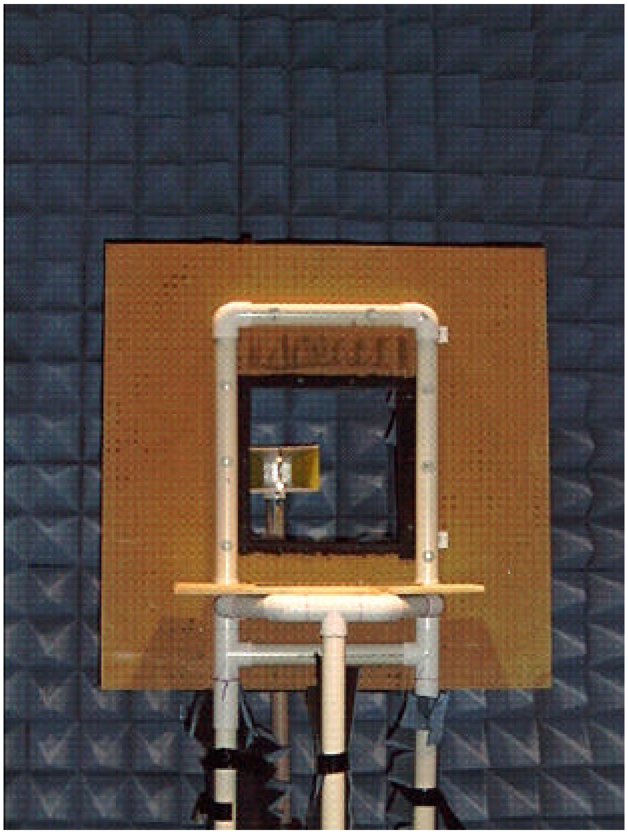

Two reference measurements were made, one with the sample holder empty and one with a plate of copper in the sample window, which were followed by the measurement of all other materials. In the data analysis section below, the reference measurements are used under some invariance assumptions to isolate the line-of-sight through material propagation path from the other unwanted components of the scattering parameter measurements.

An important parameter in the theoretical model of Section 3 is the thickness of the sample under test. The thickness of all samples was measured using digital calipers or a micrometer.

5. Analysis Method

As mentioned above, the data measured by the ANA is the scattering parameters of the cascaded network between antenna connection points. To calculate the scattering parameters of the sample alone we need to remove the effect of the antennas and any unwanted propagation paths from the measurement. We can effect this removal by using a combination of subtraction of the reference measurements and time domain gating.

If the scattering parameter of interest is considered as a frequency domain transfer function between two voltages, by taking the IFFT of the gathered frequency data we get the effective "impulse response" of that function.

$$X(f)W(f) \leftrightarrow x(t) * w(t) \tag{6}$$

where X(f) is the infinite frequency transfer function, W(f) is some window with amplitude zero outside of the observed frequency range, $x(t) = \Im^{-1}\{X(f)\}$ and $w(t) = \Im^{-1}\{W(f)\}$ are inverse Fourier transforms of their respective capitalized frequency functions, and "*" denotes convolution. x(t) is the true impulse response of the function under consideration, but we observe only the convolution of it with the function w(t). The width of w(t) will determine the resolution with which we can distinguish discrete events in the time domain – for example in S22 between reflection at the antenna and reflection from the dielectric material. The width of w(t) is inversely proportional to the width of W(f), therefore it is desirable to observe as wide a frequency range as possible. Given the time domain "impulse" response of the parameter, we can compare the response of the material under test to the response of the two reference measurements – the empty frame and the copper plate. The first 10ns of the reflection parameter impulse response for the copper plate are shown overlaid on the response for the empty frame in Figure 7, and the equivalent plot for 7mm plexiglass is shown in Figure 8. A rectangular W(f) was used.

Figure 7: Time Domain Reflection Response on the Copper Place Compared to an Empty Sample Window

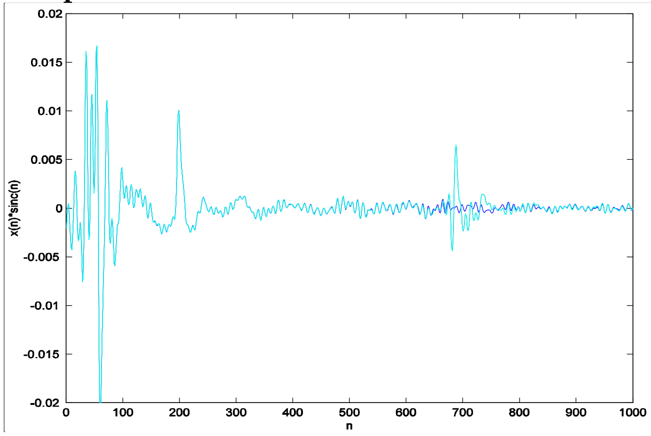

Figure 8: Time Domain Reflection Response of Plexiglass Compared to an Empty Sample Window

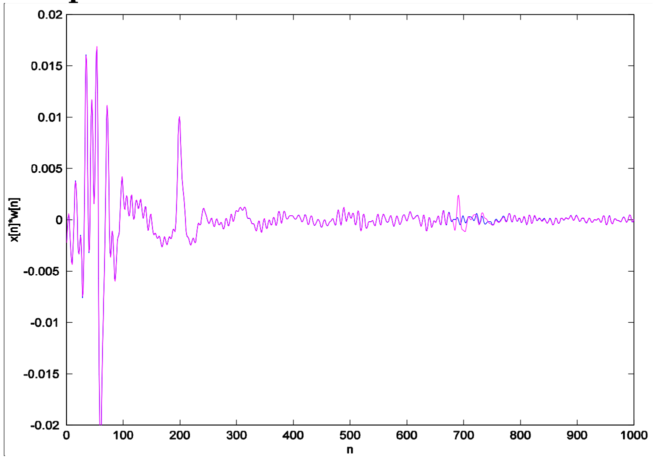

In these plots the reflection due to the sample is clearly distinguishable from the reflections due to the cable-antenna and antenna-air mismatch, the latter remaining constant in each measurement. Isolating this reflection from the other events and transforming it back into the frequency domain is done in three steps. First, the baseline time domain response of the empty frame is subtracted from the response of the sample under test, as a first pass attempt to remove unwanted reflections. Second, performance is improved by subsequently multiplying the resulting response by a time window that is zero outside of the region where the sample response is observed to deviate significantly from the baseline response, thus entirely eliminating those reflections sufficiently removed in time from the reflection due to the sample. Finally, an FFT of the resulting baseline-removed, time-windowed response is taken to get the frequency response of the isolated sample. Mathematically,

$$\begin{aligned} y(t) &= [(x(t)-b(t))*w(t)]g(t) \\ Y(f) &= [(X(f)-B(f))W(f)]*G(f) \end{aligned} \qquad (7)$$

where b(t)*w(t) is the baseline empty frame response and g(t) is the time domain window function. From Equation (3) we see that to minimize distortion in the frequency domain we should choose W(f) to be rectangular and g(t) to be some shape that minimizes ringing in the frequency domain. A Hamming window was chosen for g(t). The duration of g(t) was chosen to be just long enough to fully include the time domain response of the copper plate, specifically from the 630th to the 880th time domain sample. Because multiplication by a window in the time domain results in convolution by a window in the frequency domain, the effective result is averaging over frequency. This introduces some edge effects into the frequency domain data where the window begins to extend beyond the range of frequency data, reducing the useful frequency range.

A similar procedure was used for the transmission measurement, except there was no baseline measurement for the S_{12} data, i.e., no measurement of the isolation between ports 1 and 2. The greater propagation distances involved in an S_{12} measurement result in lower amplitudes and greater time separation for waves arriving by non-direct propagation paths, therefore a baseline is at the least less important for this case and can, in fact, increase measurement error if insufficient noise averaging is performed [21].

These procedures remove all unwanted propagation paths from the observation, but the remaining data still includes filtering due to the antennas and free space propagation, as well as reflection/transmission at the sample. To obtain the response of the sample alone, we divide by the response of the empty frame or copper plate for the transmission and reflection data, respectively. In this way, the empty frame is defined to have a transmission coefficient of 1, the copper plate to have reflection coefficient of 1, and the coefficients of all other samples are determined relative to these. Finally, because the transmission, reflection, and absorption coefficients must sum to 1, we can determine the absorption from the two calculated parameters.

To verify the obtained frequency curves for each material, we use the models relating scattering parameters to relative permittivity and loss tangent described in Section 3. By finding the value of complex permittivity that best fits the curve of the transmission parameter, in a mean square error sense, we can check that the shape of the obtained curve fits the physical model of the system, and compare the obtained complex permittivity to reference values in the literature.

5.1 Sources of Error

There are many points in the measurement and analysis where error can enter the data, although every effort is made to minimize such error. In the measurement of data, the most significant source of potential error is the test rig itself. The substructure of the rig is made from PVC, which will bend under weight and even sag under its own weight over a period of time, particularly when there are many joints in the structure. The result being that the position of sequential samples may not be exactly the same relative to the antennas being used to measure them. In addition, the test rig is not firmly attached to the ground, and is therefore susceptible to accidental movement in the placing and removal of sample specimens.

There is also the question of transmitted energy due to diffraction around the sample. In several cases the unusual shape of the specimen made it difficult to ensure that the test material was in contact with the back of the frame on all sides, allowing the possibility of significant wave propagation around the sample. For materials where the sample was constructed from a number of un-bonded pieces, specifically the red brick, cinder block, fiberglass, and 2x12 Fir lumber, there is also the possibility of wave propagation through the air gaps between pieces.

The test rig was placed close to the transmit antenna in order to minimize distortion to the incident wave due to blockage of the Fresnel zone, i.e., minimizing the effect of wave diffraction as it passes through the window. However, the close proximity makes it more difficult to isolate the reflected signal due to the sample from the reflection due to the antenna. Furthermore, the incident wave less closely approximates a plane wave at the sample interface than if the antenna - sample separation was greater. The plane wave approximation is important when comparing results to the theoretical model of Section 3.

We attempt to remove the unwanted artifacts, such as antenna reflection, from the raw data by subtracting the baseline measurement, and then multiplying by a time window. Subtracting the baseline measurement assumes that the response of the system within the window is time-invariant, except for the response due to the sample. However, there will be some variation due to potential movement of the test rig, as described above, and variations that occur due to non-ideal cables and connectors in the test setup. Windowing the data will unavoidably include some of the residual baseline variations and/or exclude the vestiges of the desired data. The reflection parameter data in particular was observed to be sensitive to the choice of window.

Division by the reference measurements to determine the relative coefficients implicitly assumes the network behaves linearly. That is, it assumes that the combined effect of the antennas, free-space propagation, and reflection at the sample can be described as a time-invariant multiplication by a complex gain function. This is, however, considered to be a reasonable assumption.

Finally, the samples were generally not of uniform thickness. The measured values described below and used in the model are either sample, or average thicknesses of the materials.

5.2 Results

Data was measured from 1 – 12GHz, however, because of edge effects due to time domain windowing, and lack of reliability due to cable losses at higher frequencies, results are only reported for the frequency range 2 – 7GHz.

The list of materials considered is given in. The first material tested was the 7.1mm plexiglass, the relative permittivity of which is known to be stable over frequency and well reported in the literature. Plots of the power transmission, reflection, and absorption coefficients are shown in Figure 10. Note that the theoretical curves for the transmission coefficient match the observed value more closely than those for the reflection coefficient, this is typical for all the materials and is due to a number of factors. Based on the equations in Section 3, it is possible to estimate the relative permittivity of the material under test using either the measured transmission or reflection coefficient. In general, using the transmission coefficient to find relative permittivity was found to provide a better subsequent match to the reflection coefficient curve than vice versa, therefore this was the method was used. Naturally, the match to the curve on which the estimate was based is better. In [19] it is suggested that use of the reflection coefficient would be the optimal choice for high-loss materials, which we are not generally dealing with here. Also, the value of the S_{22} is up to an order of magnitude smaller than S_{12}, resulting in an increased fractional variation due to observation and processing noise. The absorption coefficient is generally an order of magnitude smaller again, resulting in even more variation in that curve. Missing data in the absorption curve indicates calculated absorption of zero.

Table 1: Materials Under Test

Material	Comments
Plexiglass	7.1mm and 2.5mm thicknesses tested
Blinds	Mini-blinds, slats 25mm wide, 0.5mm thick. 22mm openings.
Red brick	Each brick approx. 203mm (w) x 51mm (h) x 102mm (d). 17 stacked.
Carpet	Cheapest available, 7.75mm thick
Ceiling tile	Typical of false ceilings in office buildings. 14.7mm thick.
Fabric	Heaviest available upholstery, 1.13mm thick.
Fiberglass	R-13 for interior and exterior walls in warm climates, 890mm thick.
Glass	Window glass, 2.5mm thick.
Drywall	Nominally 12.8mm and 9mm, thinner sample varied from 8.5mm to 9.9mm over sample.
Light cover	For fluorescent light bays in office buildings, approx 0.5mm wide diamond corrugations, thickness varies between 2.3 – 2.7mm over corrugations.
Linoleum	Cheapest available, 1.61mm thick.
Fir lumber	Two boards stacked vertically. E-field perpendicular to grain, 37.7mm thick.
Particle Board	19mm thick
Plywood	5 sheet plywood, total thickness 18.28 – 18.45mm over sample.
Tiles	Tiles were approx. 10.8 x 10.8 x 7.3 mm, glued to 12.8mm drywall with gaps grouted. Total thickness approx 21.2mm
Tar paper	1.7mm thick.
Cinder block	Blocks approx. 406mm (w) x 203mm (h) x 194mm (d) outside dimensions, construction is 4 exterior "walls" and 1 cross member bisecting widest dimension, wall thickness 31-35mm. Three vertically stacked.
Diamond mesh	5mm wide "v"-shaped ribs every 25mm, 8 "diamonds" between them. Diamonds approx. 13mm x 6mm. E-field perpendicular to ribs. Rib "v" depth 8.5mm, metal thickness 2mm.
Stucco	Concrete poured on diamond mesh. Orientation as above. Total thickness 25.75mm.
Wire lath	51mm x 51mm spaced lattice of 16 gauge wire (1.56mm), paper backed (0.95mm).

It is important to note that the estimate of relative permittivity was chosen to provide the best fit across the frequency range, whereas in reality the permittivity of many materials is a function of frequency. This can have significant effect on the closeness of the fit between the measured and estimated curves.

The calculated value of relative permittivity and loss tangent for each material, and a comparative reference value are shown in Table 2 on the next page.

Table 2: Relative Permittivities and Loss Tangents

Material	Est. e_r	Est. tand	Reported e_r	Reported tand	Ref.
Plexiglass (7.1mm)	2.74	3.20E-04	2.59	57e-4	[10]
Plexiglass (2.5mm)	2.50	9.37E-03	2.59	57e-4	[10]
Blinds (closed)	3.49	5.96E-05			
Blinds (open)	1.96	5.96E-05			
Red brick (dry)	5.86	1.16E-01			
Red brick (wet)	5.92	1.17E-01			
Carpet (back)	1.31	6.69E-04			
Carpet (weave)	1.32	5.96E-05			
Ceiling tile	1.32	1.44E-02			
Fabric	1.49	5.96E-05			
Fiberglass	1.02	9.21E-04	3.9	0.026	[10]
Glass	6.38	2.60E-02	4.05	0.0106	[22]
Drywall (12.8mm)	2.19	1.11E-02			
Drywall (9mm)	2.49	4.25E-03			
Light cover (front)	1.66	6.88E-03			
Light cover (back)	1.64	1.19E-02			
Linoleum (back)	3.04	6.31E-05			
Linoleum (front)	3.08	1.45E-03			
Fir	2.58	2.00E-01	1.7-3.8	0.022-0.26	[23]
Particle Board	2.70	1.10E-01	2.7-3.07	0.07-0.09	[23]
Plywood	2.47	1.27E-01	1.7	0.036	[22]
Stucco (back)	7.30	4.45E-01			
Stucco	1.07	4.29E-			

Material	Est. e_r	Est. tand	Reported e_r	Reported tand	Ref.
(front)		01			
Tiles	3.08	5.88E-02			
Tar paper	2.47	3.86E-02			

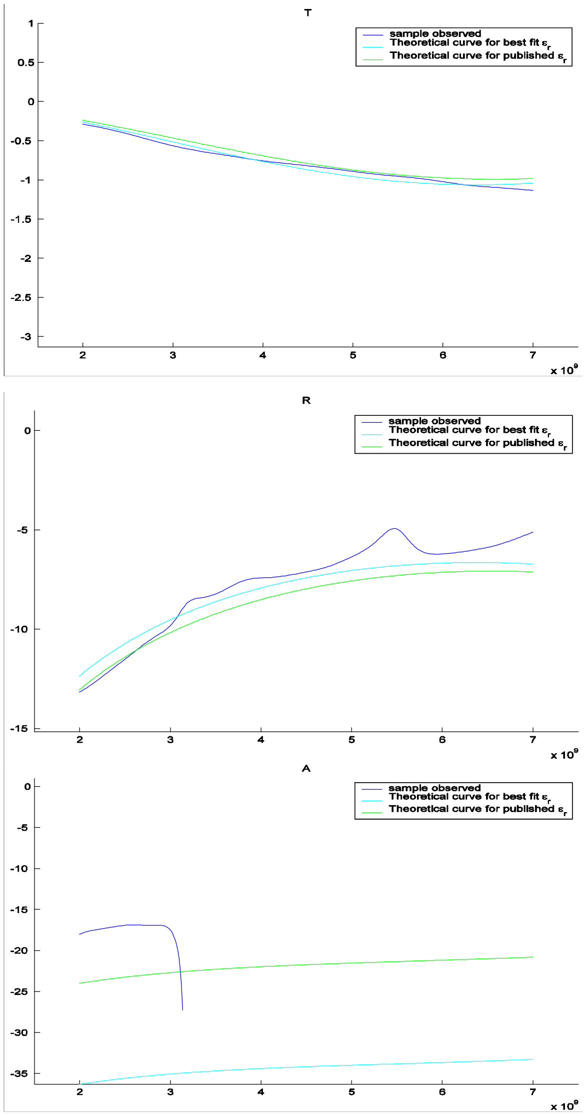

Figure 10: Transmission, Reflection and Absorption Coefficients for 7.1mm Plexiglass

For the wood products, the parameters are a strong function of moisture content and a range of reference values for 0-30% moisture content is given. For materials tested in more than one orientation, the side indicated in brackets () is the side facing the transmit antenna.

In Table 3, the transmission and reflection coefficient of each material is given at 2.3GHz and 5.25GHz, along with the center frequencies of each band of interest, and the difference in coefficient between frequencies.

Table 3: Transmission and Reflection Coefficients at 2.3GHz and 5.25GHz

Material	T (dB)			R (dB)		
	2.3 GHz	5.25 GHz	Δ	2.3 GHz	5.25 GHz	Δ
Plexiglass (7.1mm)	-0.3560	-0.9267	0.5707	-12.23	-5.65	-6.5753
Plexiglass (2.5mm)	-0.0046	-0.2041	0.1994	-21.69	-13.25	-8.4470
Blinds (closed)	-0.0016	0.0020	-0.0035	-30.97	-20.39	-10.578
Blinds (open)	0.0137	0.0315	-0.0178	-44.23	-46.95	2.7210
Red brick (dry)	-4.4349	-14.621	10.186	-12.53	-8.98	-3.5459
Red brick (wet)	-4.5119	-14.599	10.087	-12.52	-9.41	-3.1185
Carpet (back)	-0.0361	-0.0318	-0.0044	-25.19	-15.8	-9.4080
Carpet (weave)	-0.0271	-0.0056	-0.0214	-26.94	-18.7	-8.2710
Ceiling tile	-0.0872	-0.1795	0.0923	-21.07	-18.7	-2.3470
Fabric	0.0216	0.0133	0.0083	-41.70	-30.1	-11.570
Fiberglass	-0.0241	-0.0340	0.0099	-39.40	-28.8	-10.581
Glass	-0.4998	-1.6906	1.1908	-11.29	-4.9	-6.3446
Drywall (12.8mm)	-0.4937	-0.5149	0.0211	-12.11	-11.5	-0.6390
Drywall (9mm)	-0.5095	-0.8470	0.3376	-12.03	-8.87	-3.1596
Light cover (front)	-0.0040	-0.0533	0.0494	-28.47	-20.0	-8.4490
Light cover (back)	-0.0070	-0.0532	0.0462	-28.07	-18.8	-9.2390
Linoleum (back)	-0.0186	-0.1164	0.0977	-26.05	-17.3	-8.7610
Linoleum (front)	-0.0198	-0.1278	0.1081	-23.69	-16.0	-7.6690
Fir lumber	-2.7889	-6.1253	3.3364	-17.45	-14.8	-2.6890
Particle Board	-1.6511	-1.9508	0.2997	-8.59	-14.1	5.5359
Plywood	-1.9138	-1.8337	-0.0801	-9.05	-30.5	21.422
Stucco (back)	-14.582	-13.906	-0.6760	0.62	0.04	0.5785
Stucco (front)	-14.863	-13.235	-1.6280	-2.38	-9.24	6.8587
Tiles	-2.2163	-1.4217	-0.7946	-6.24	-14.9	8.6093
Tar paper	-0.0956	-0.1341	0.0385	-28.88	-17.8	-11.067
Cinder block (dry)	-6.7141	-10.326	3.6119	-7.67	-6.13	-1.5324
Cinder block (wet)	-7.3527	-12.384	5.0313	-5.05	-7.55	2.5080
Diamond mesh	-20.985	-13.165	-7.8200	-0.53	0.89	-1.4216

Material	**T (dB)**			**R (dB)**		
	2.3 GHz	**5.25 GHz**	**Δ**	**2.3 GHz**	**5.25 GHz**	**Δ**
Wire lath (paper)	-1.2072	-0.7044	-0.5028	-6.38	-10.9	4.6015
Wire lath (wire)	-1.2136	-0.3404	-0.8732	-8.01	-21.8	13.764

Plots of T,R and A for some materials are presented below, the remainder can be found in the Appendix.

Plots for the bricks are shown in Figure 11. The bricks showed a linear increase (in dB) in absorption over frequency, with a relatively constant degree of reflection. The periodicity in the curves is a function of the thickness of the sample in this, and later figures. Lack of precise alignment in periodicity between the observed and theoretical curves can be attributed to imperfect estimation of the sample's thickness.

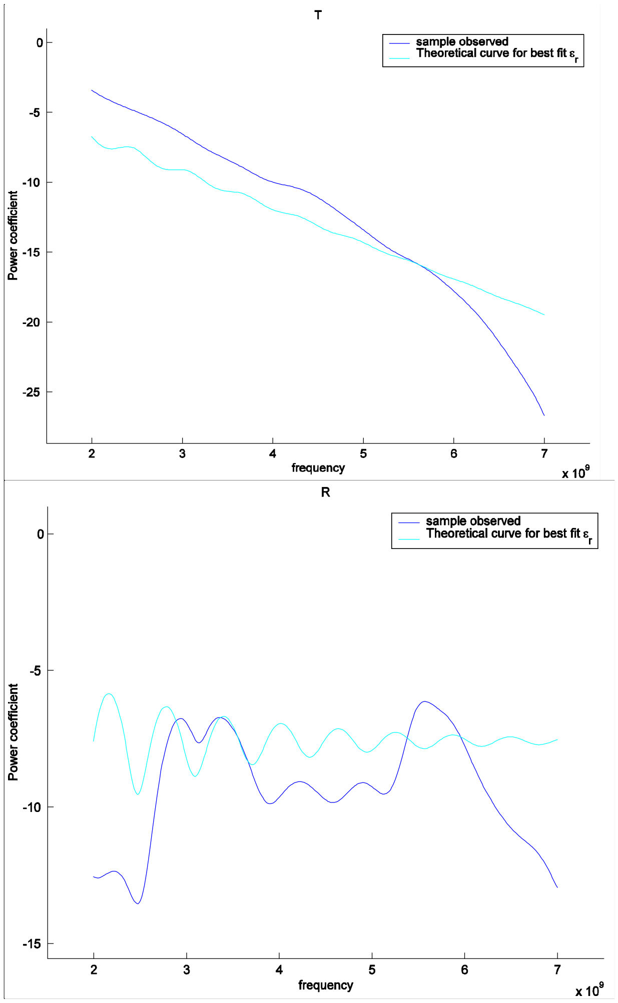

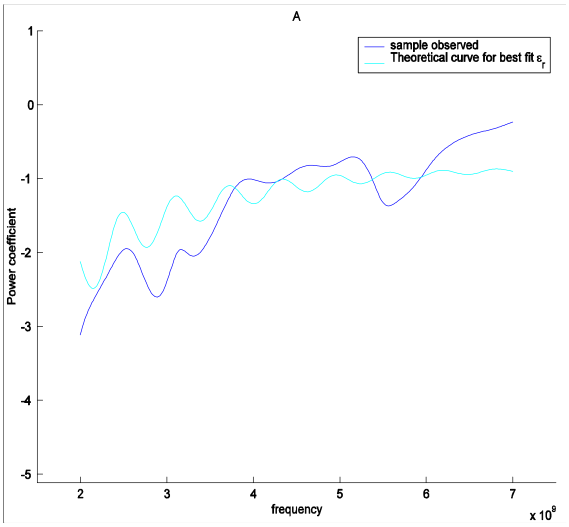

Figure 11: Coefficients for Red Brick

The sample consisted of 17 bricks stacked in the window opening, with damp paper towels filling the gaps between them, see Figure 12.

Figure 12: Sample of Red Brick, Front and Rear Views

The sudden change near 2.5GHz might be attributable to the fact that this is the resonant frequency of water. Adding a "thin water film" to the front surface of the bricks did not significantly alter the curves, as demonstrated by the figures in Table 3.The ceiling tile is of the kind typically found in office buildings, plots of the coefficients are in Figure 13.

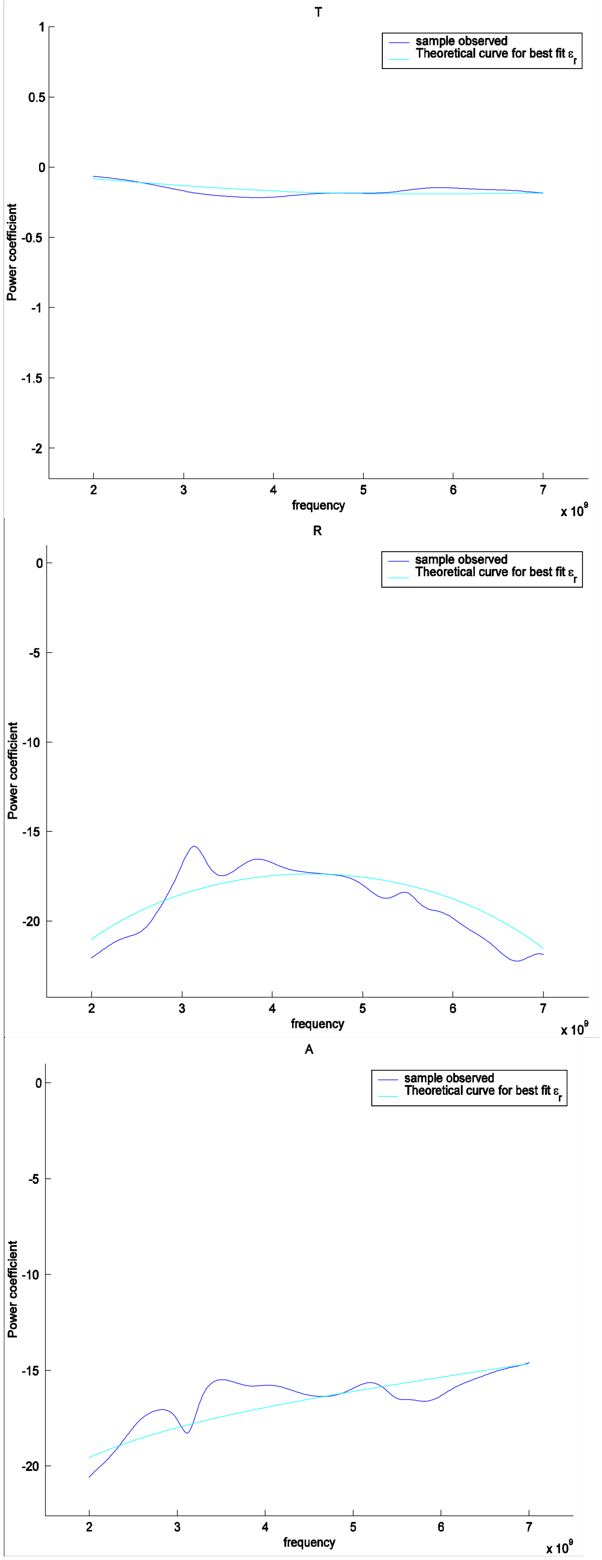

Figure 13: Coefficients of Ceiling Tile

The ceiling tile is shown in the test rig in Figure 14.

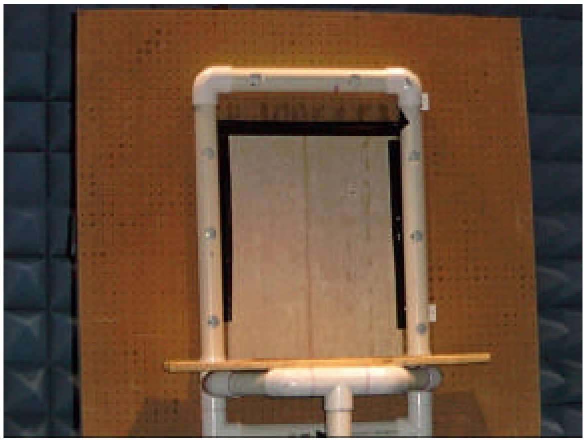

Figure 14: Ceiling Tile Test Setup

The fiberglass sample was devised from two R13-rated, 3.5 inch thick blocks, placed side by side, as shown in Figure 15. Its recommended use is for interior walls and exterior walls in warm climates. It showed a particularly poor match to the estimated and reference permittivity curves, shown in Figure 16.

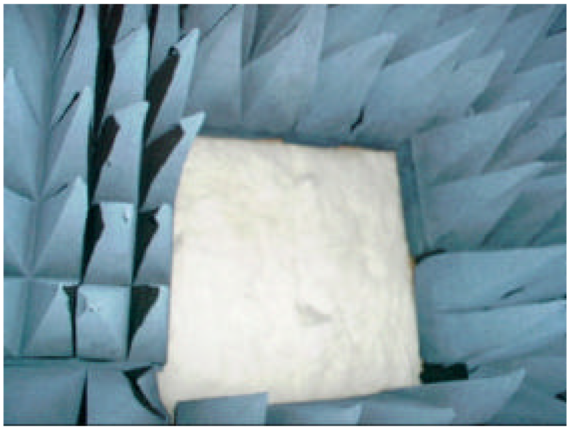

Figure 15: Fiberglass

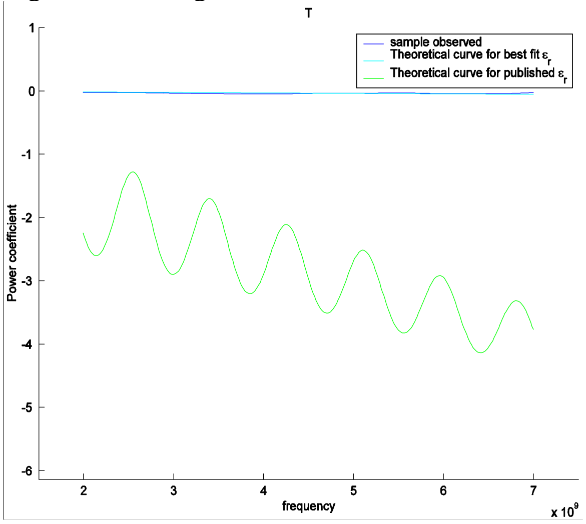

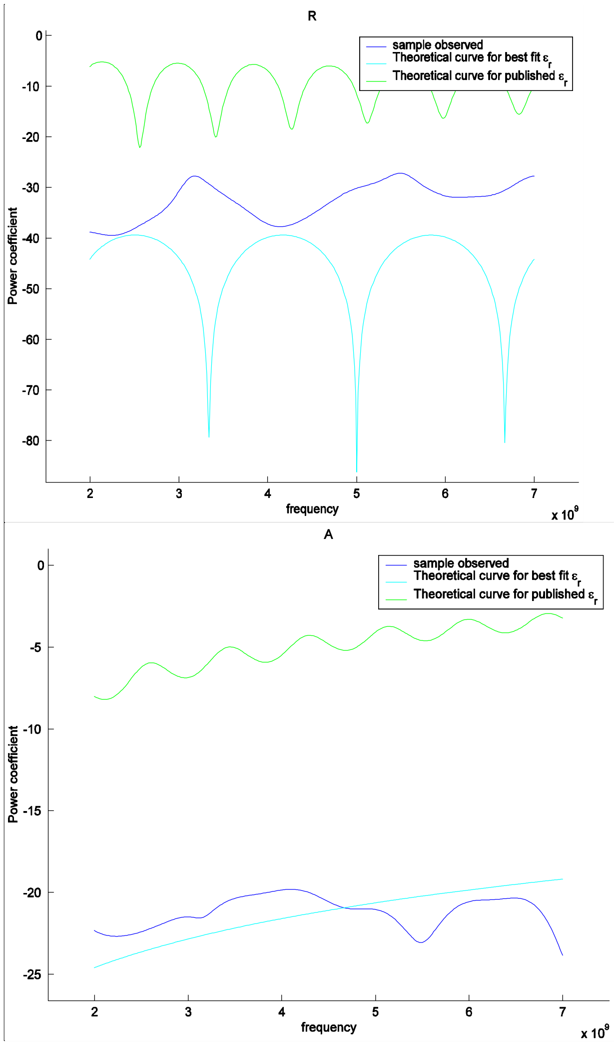

Figure 16: Fiberglass Coefficients

The reference curve, with relative permittivity taken from [10], is specifically for fiberglass with 40% glass. The glass content of the fiberglass in this case is not known. The measured complex permittivity was 1.02(1+j0.0009), indicating very little resistance to wave propagation and low reflection values. The large decibel deviation in reflection coefficient between measured and theoretical curves can be explained by the increased fractional error at low power, as discussed above.

The drywall demonstrated very little change in transmitted power across the frequency range, as shown in Figure 17 for the 13mm sample.

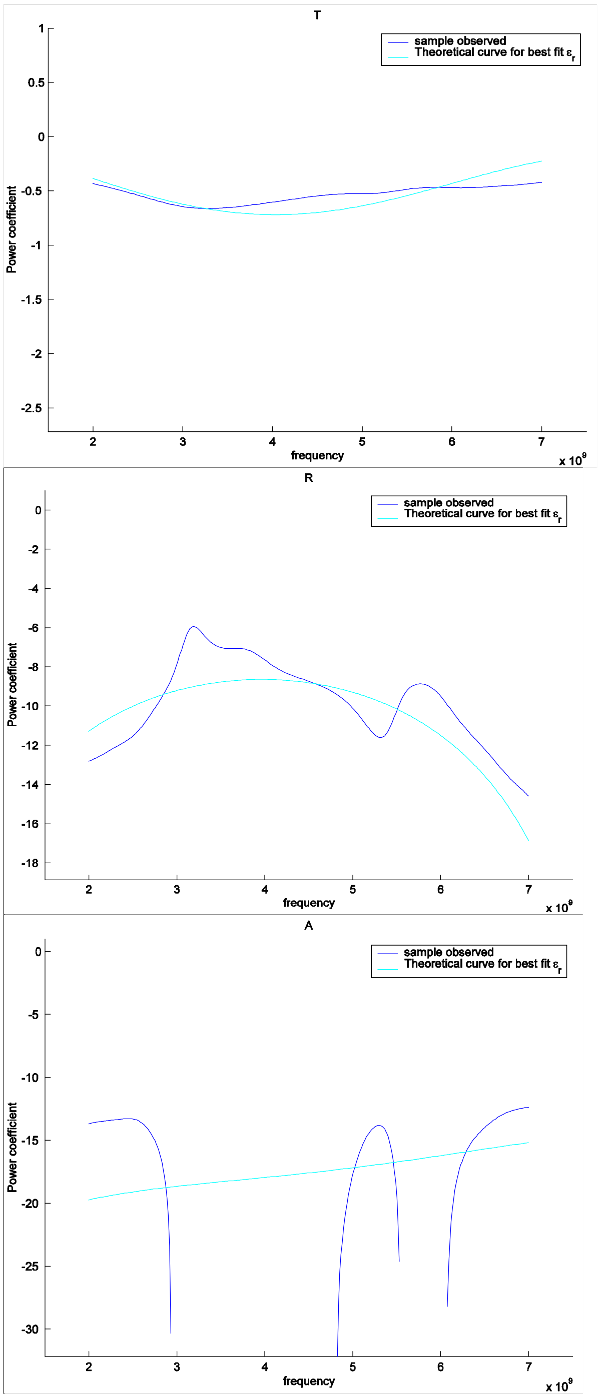

Figure 17: 12.8mm Thick Drywall Coefficients

The deviations in reflected power and lack of corresponding deviations in transmitted power near 3 and 5 GHz are unexplained, however, they are apparent in the drywall samples of both thicknesses, and the sample of bathroom tiles glued to a different 13mm drywall sample. (see Appendix).

The sample of Fir lumber was composed of two stacked blocks of 18w x 12h x 2d inches, sealed with damp paper towels, refer to Figure 18.

The coefficient curves are shown in Figure 19. As mentioned above, the relative permittivity for wood varies greatly depending on moisture content [23]. The reference curve used in these figures assumed a moisture content near 0. The estimated curve suggests the actual moisture content is closer to 20%, perhaps enhanced by the presence of the damp paper between blocks. The presence of nulls in the reflection coefficient is a function of the sample thickness. The reduction in transmitted power between 2.3 and 5.25 GHz is over 3dB.

The plywood demonstrated similar nulls in the reflection coefficient, however, the location of the null is close to 5.3GHz, corresponding to half a wavelength in the 18mm plywood, and therefore an over 20dB reduction in reflected power from 2.3 to 5.25 GHz. Note that at the reported permittivity of 1.7, as given in Table 2, the half wavelength null would be at 6.4GHz. Once again, the permittivity is a function of moisture content.

Figure 18: 2" Fir Lumber Sample

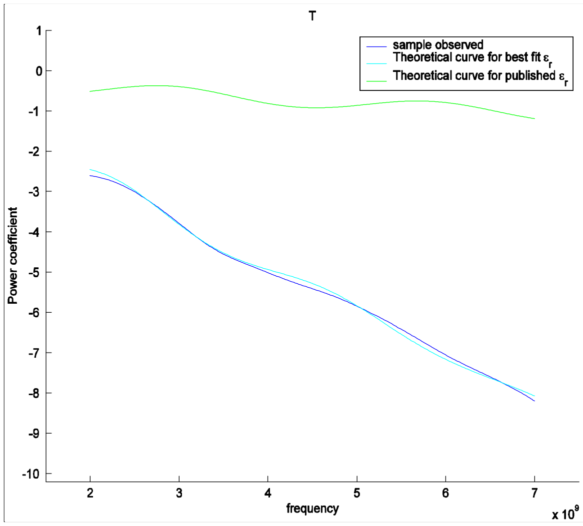

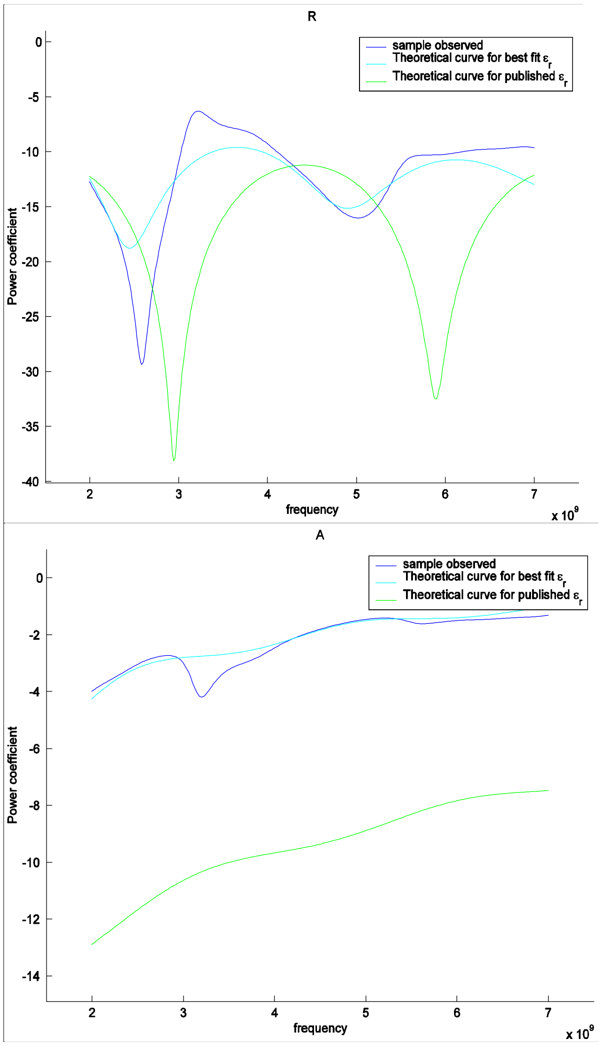

Figure 19: Coefficients of 2" Fir lumber

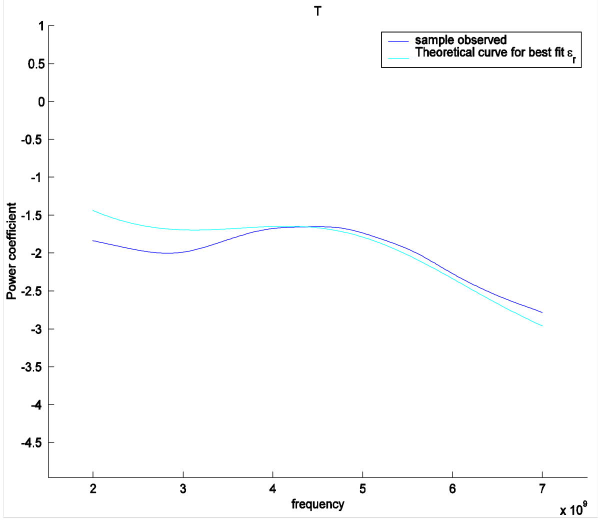

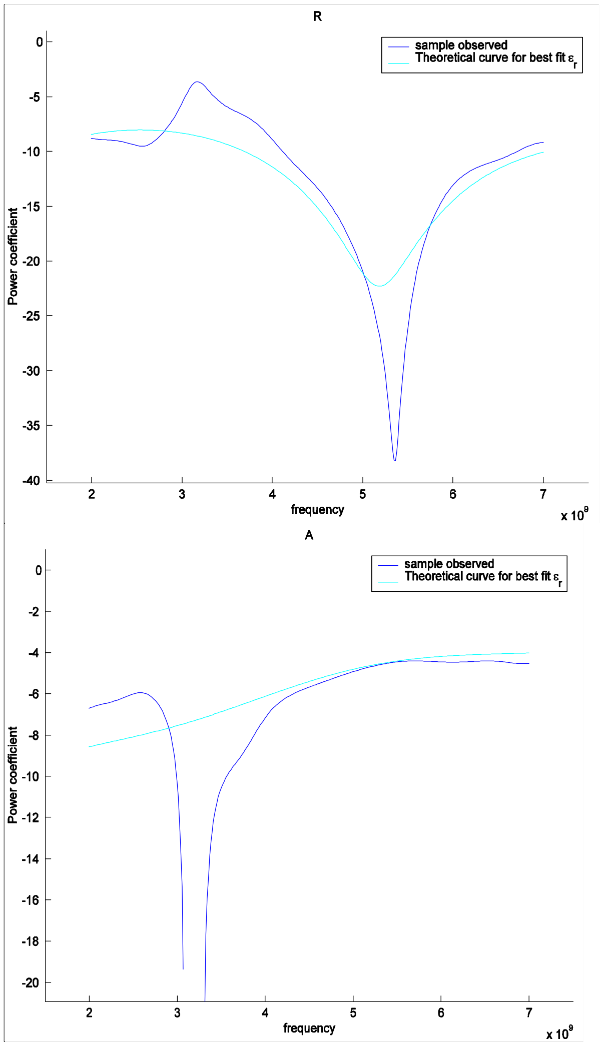

Figure 20: Coefficients of Plywood

The stucco sample is 1 inch thick concrete on a backing of steel diamond mesh, see below. In the figure the diamond mesh (back) side of the stucco is facing the transmitter, however, the plots below are for the front facing measurement. For plots of the diamond mesh on its own see the Appendix.

The small size of the gaps in the diamond mesh cause it to reflect more energy at lower frequencies. The stucco also displayed this behavior, as shown in Figure 22. However, the stucco features a null in the reflection coefficient that is not present in the diamond mesh alone, probably from the standing wave effects due to the thickness of the sample, as mentioned previously.

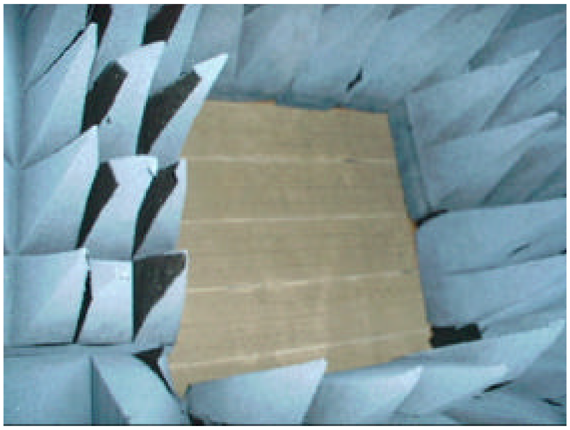

Figure 21 **Stucco Sample, Front and Back**

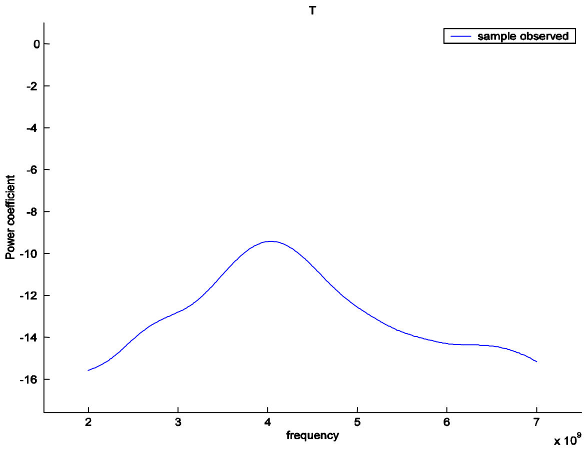

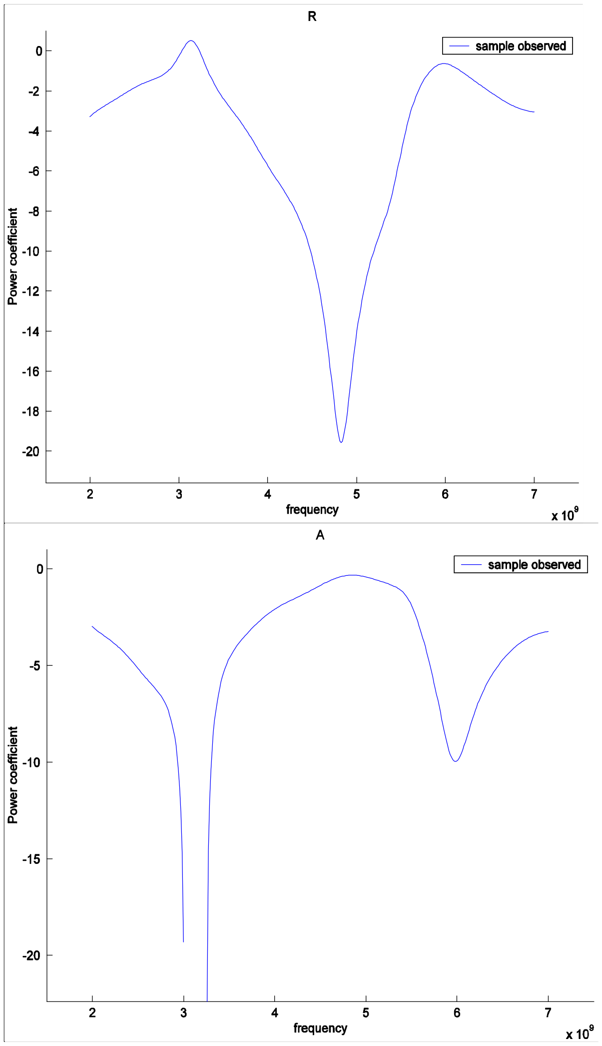

Figure 22: Coefficients of Stucco (front)

The combination of these effects results in little difference in transmitted power between 2.3 and 5.35 GHz, compared to the difference due to the diamond mesh alone.

The most complex sample is the cinder block. The large size of the blocks made it impossible to fit enough onto the sample platform to fill the window, however, the window was covered to within an inch on either side. To temporarily reduce the lateral window size, absorber material was inserted on each side. The empty frame was also re-measured with the smaller window and used as a reference for the cinder block measurement. The new measurement set up is shown in Figure 23.

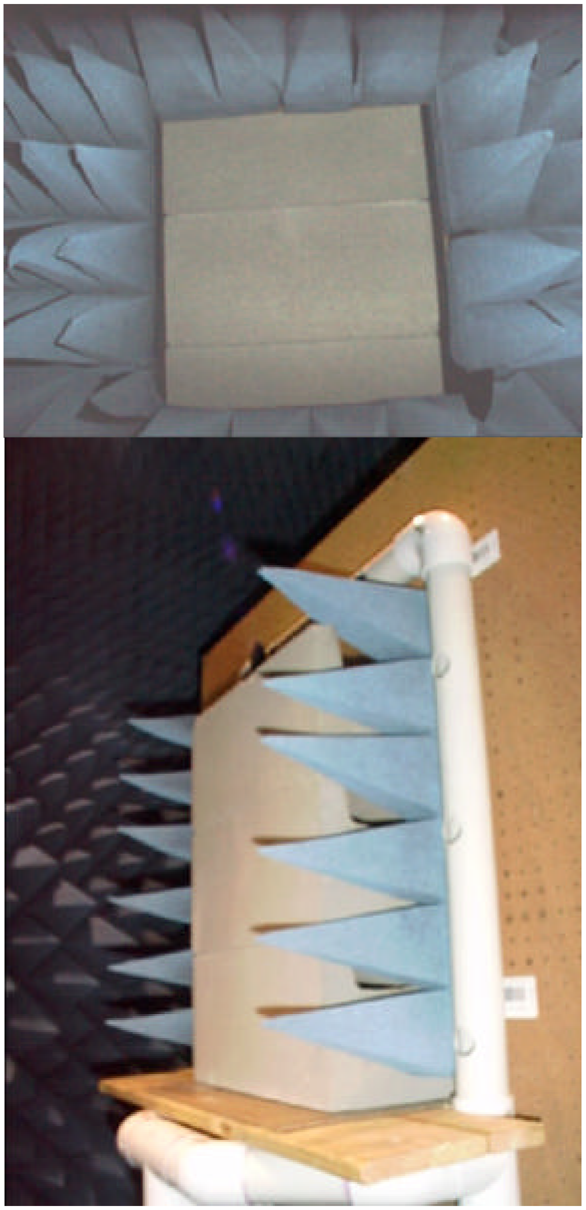

Figure 23: Modified Window Measurement Setup for Cinder Block with Added Absorber Material

The coefficient curves are shown in Figure 24. The plane-parallel plate model used for other materials is not suitable for the complex structure of the blocks [2], and no attempt was made to model the behavior. The curves reflect the expected periodicity in response due to the physically periodic structure of the material. The resulting difference between the 2 and 5 GHz bands is approximately 3dB.

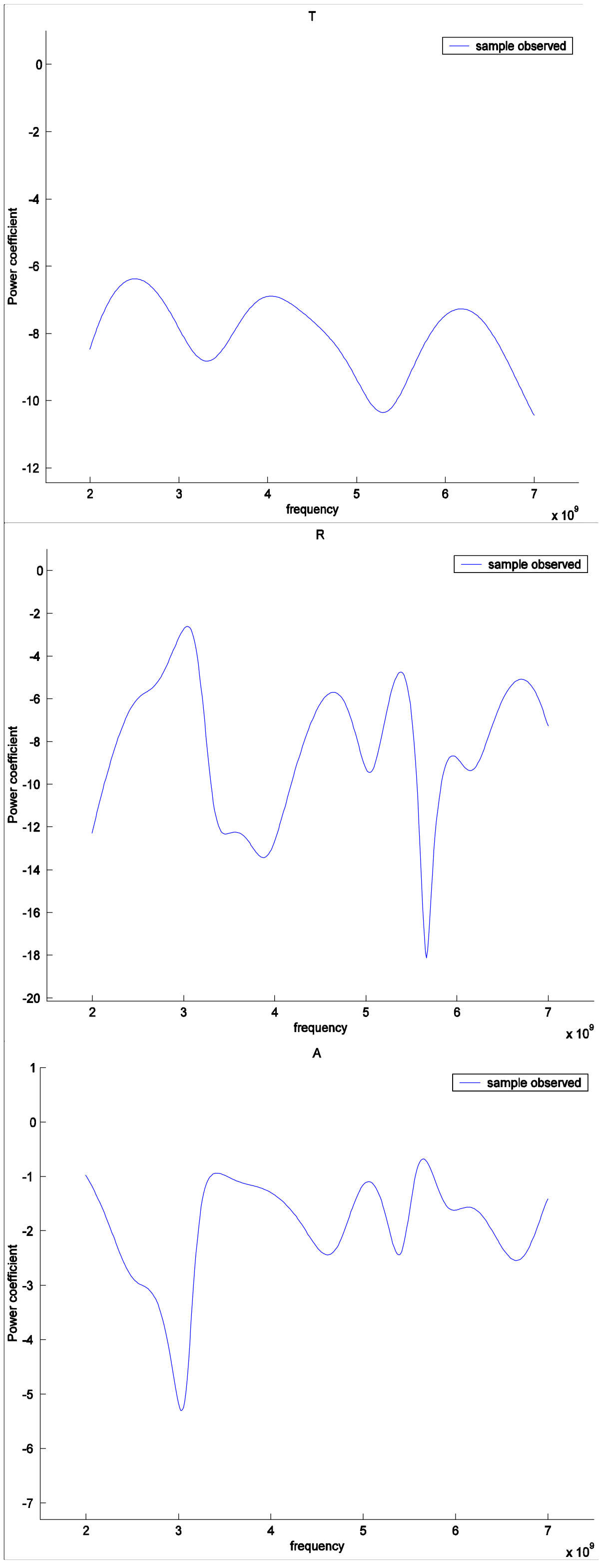

Figure 24: Coefficient Curves for the Cinder Block

6. Conclusions

Twenty materials, both homogenous and composite, have been studied to determine the variation in transmitted and reflected energy over frequency. The difference in behavior between the 2.2-2.4GHz and 5.15-5.35GHz bands is of particular interest. In order to verify the observed behavior, the measured data was used to calculate the relative permittivity and loss tangent of each material and the observed behavior compared to that of a common plane-parallel plate physical model. In most cases the observed and modeled behavior matched well, although for many materials reference values of relative permittivity and loss tangent to use as a further check have not been found.

For most materials, the decrease in transmitted power between 2.3 and 5.25 GHz is less than 1 dB, the exceptions being red brick (10.1dB), glass (1.2dB), 2 inch Fir lumber (3.3dB), cinder block (3.6dB), and stucco (increased 1.6dB). The variation in reflected power is more variable in a relative sense, due to the generally lower reflected energy. Reflected energy also shows a strong frequency dependence that is a function of the thickness of the sample, as well as its permittivity.

7. Looking Ahead

An upcoming Magis white paper will utilize the results of this report,, in addition to other theory and field measurements, to develop a number of advantages that operation at 5 GHz has over operation at 2.4 GHz. These advantages go well beyond spectrum issues (e.g., microwave ovens, 2.4GHz cordless phones, etc.) that are problematic at 2.4 GHz. Range and throughput performance results in non-line-of-sight case studies will be reported that far exceed the performance reported to date for 802.11a and 802.11b systems.

8. Appendix: Measurements

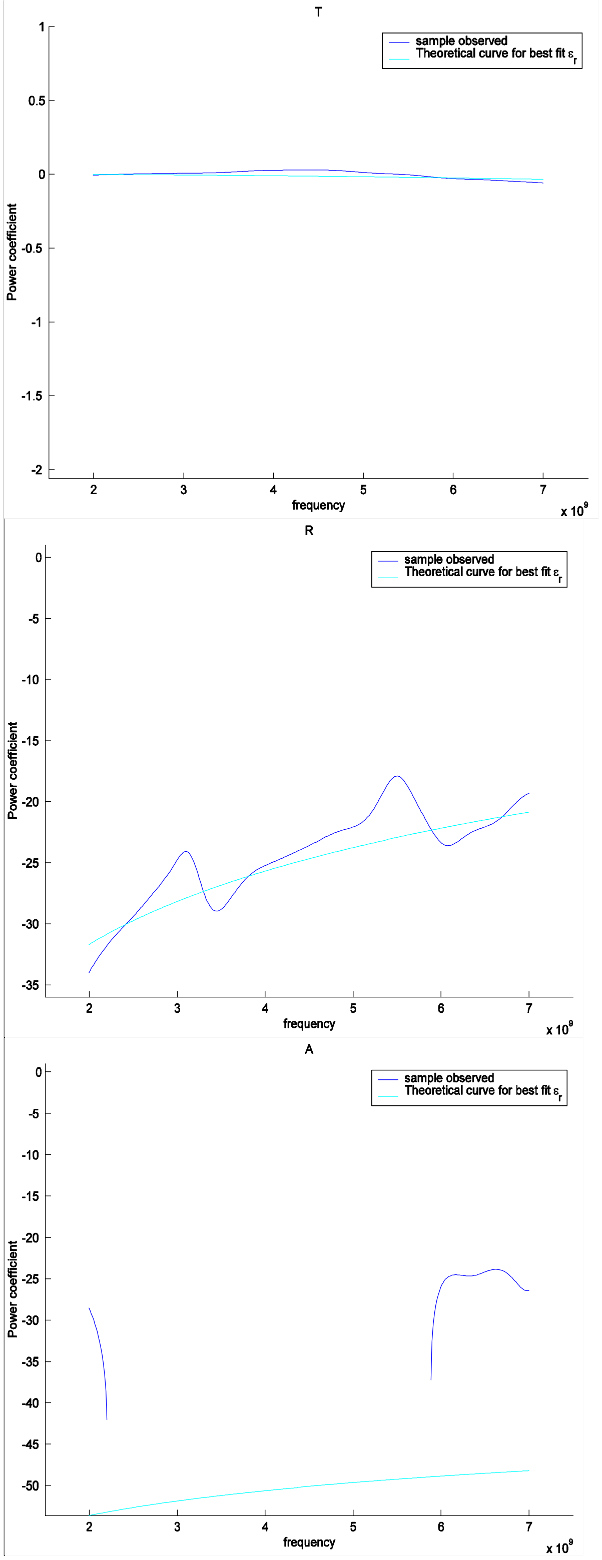

Figure 25: Blinds (Closed)

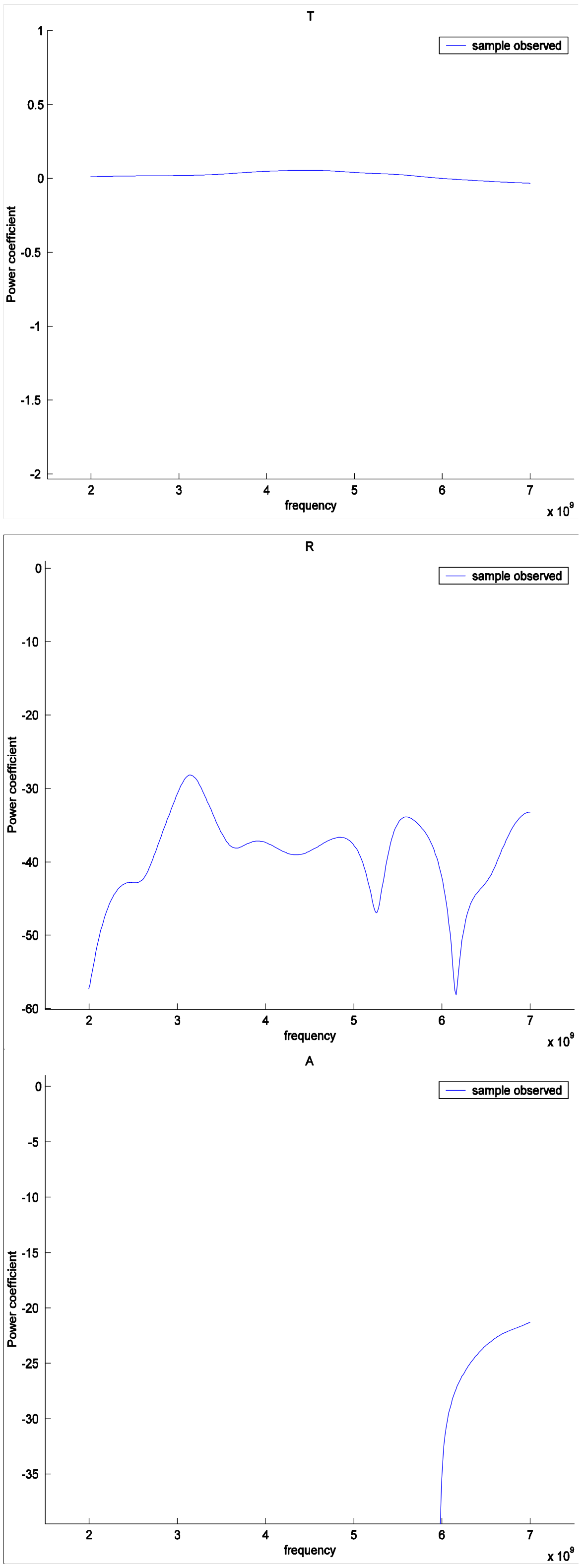

Figure 26: Blinds (Open)

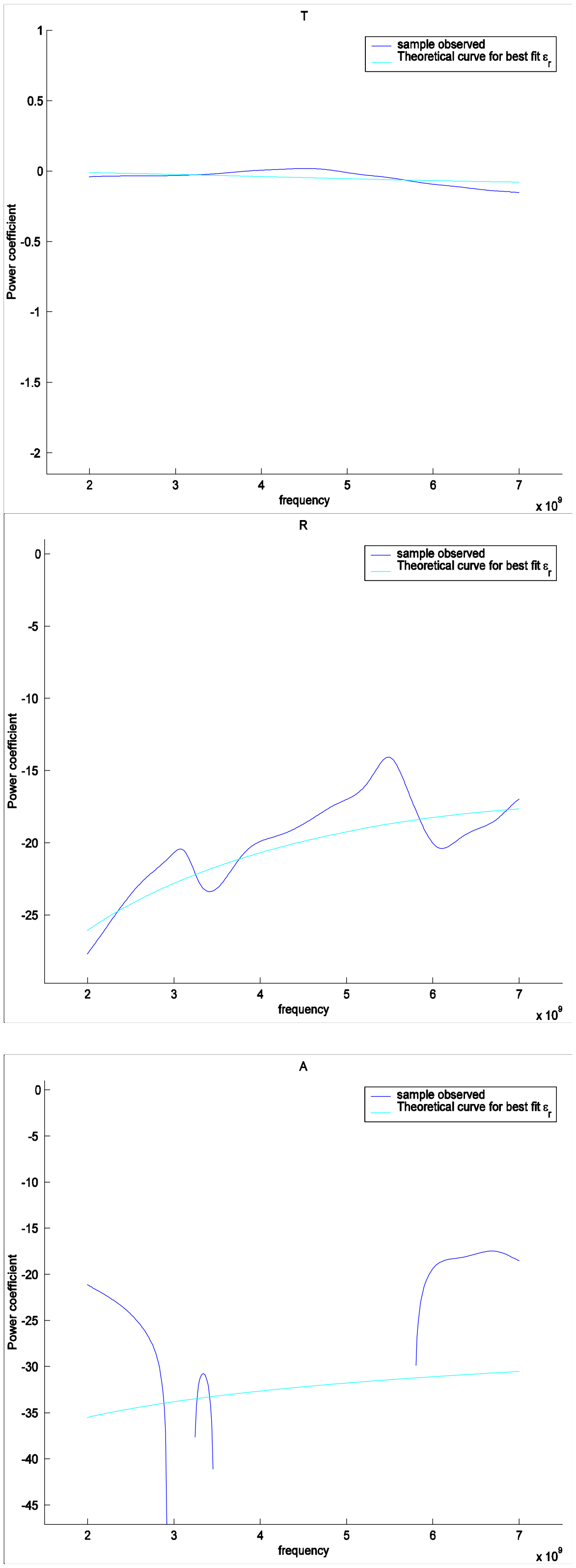

Figure 27: Carpet (Back)

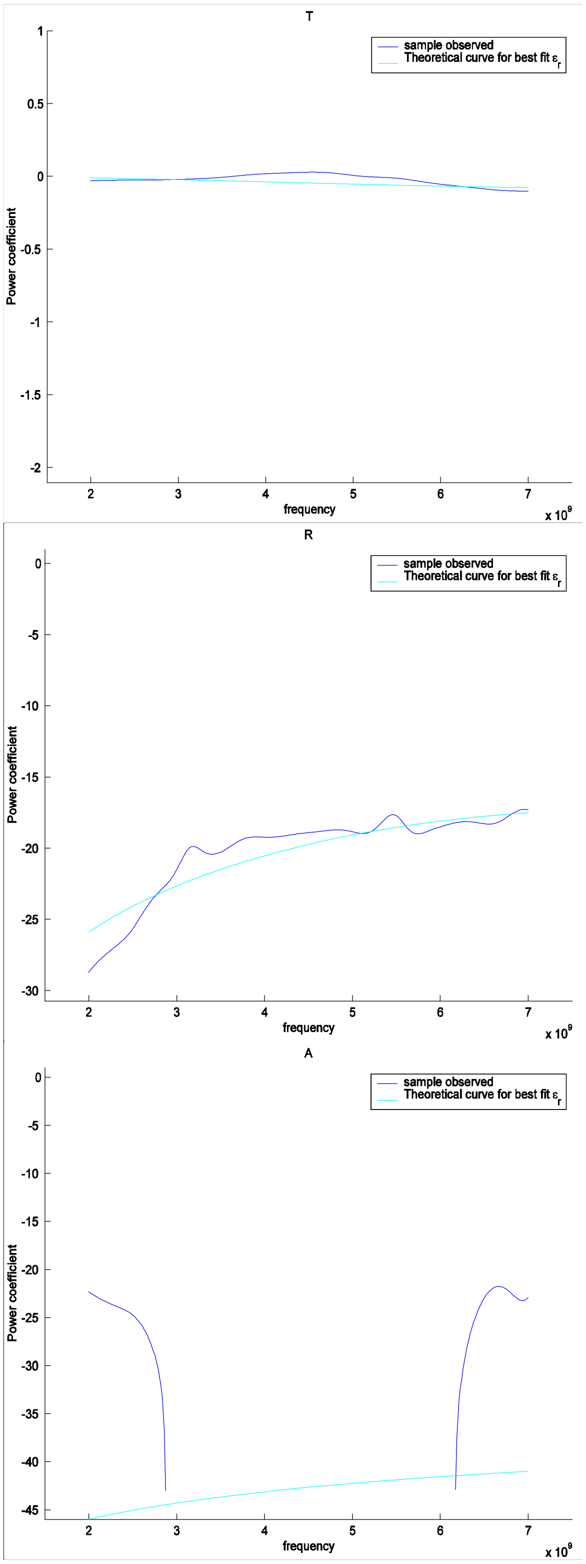

Figure 28: Carpet (Front)

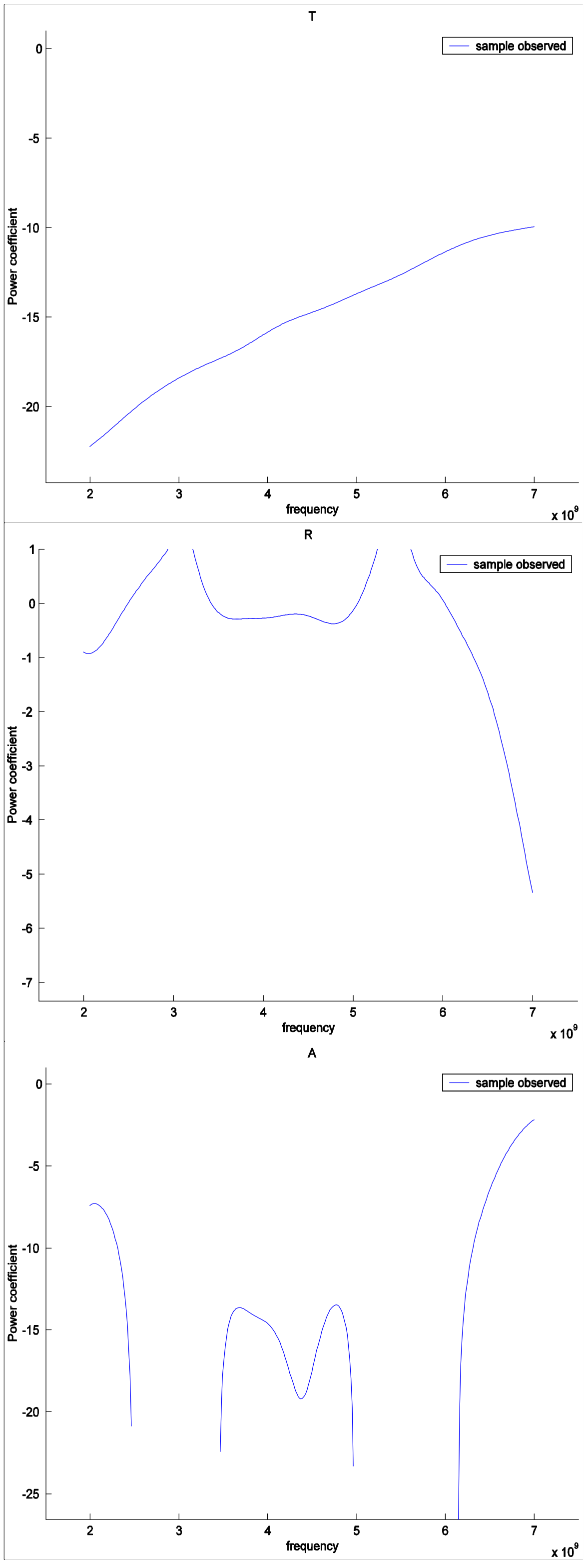

Figure 29: Diamond Mesh (for Stucco)

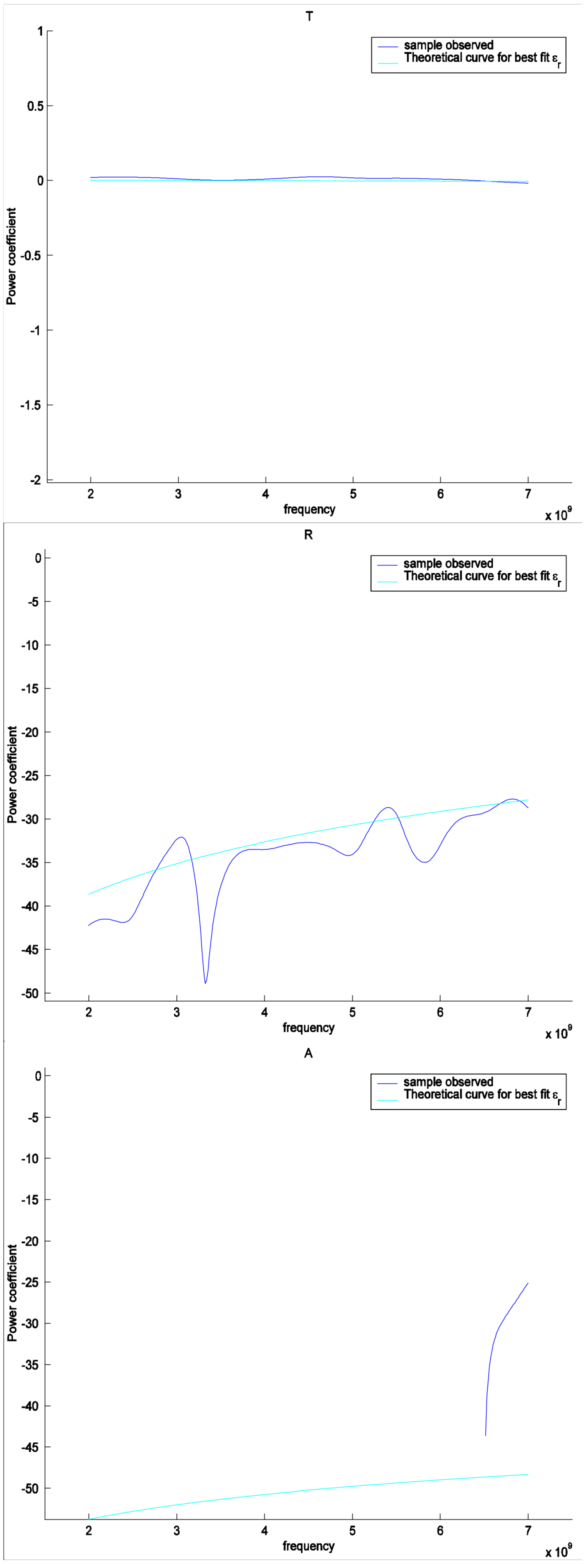

Figure 30: Heavy Fabric

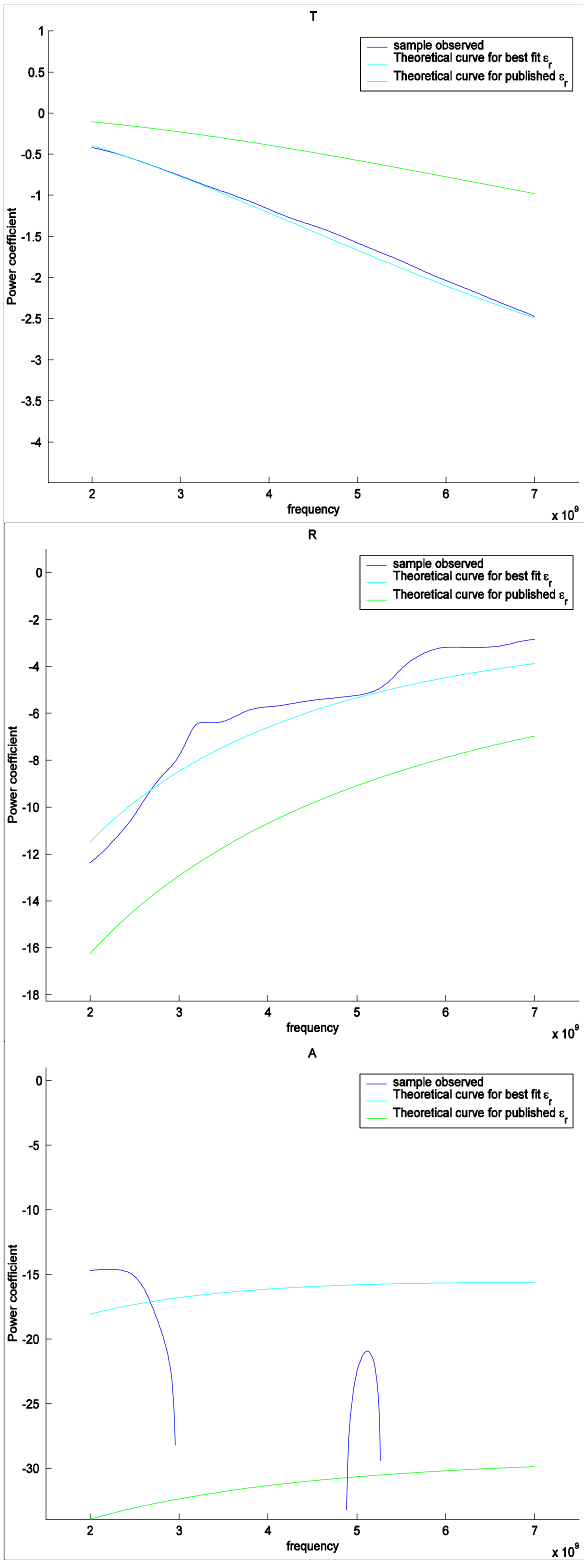

Figure 31: Glass

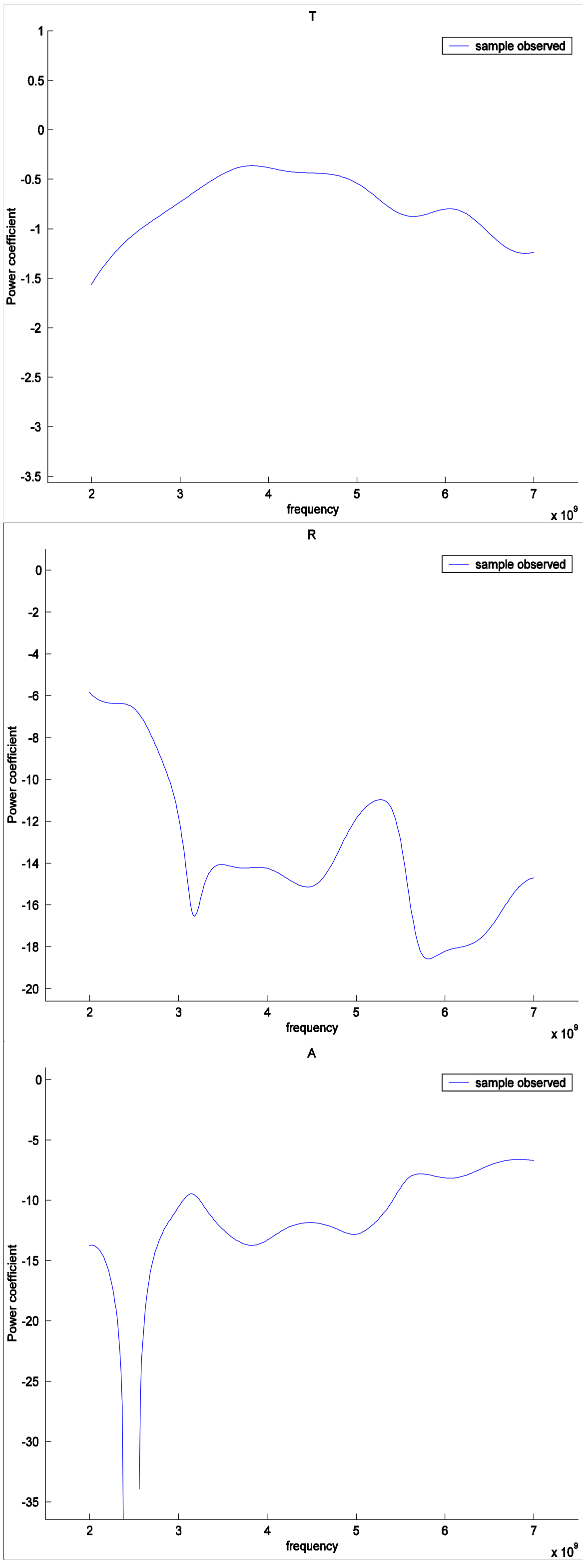

Figure 32: Paper Backed Wire Lath (for Stucco, Paper Side)

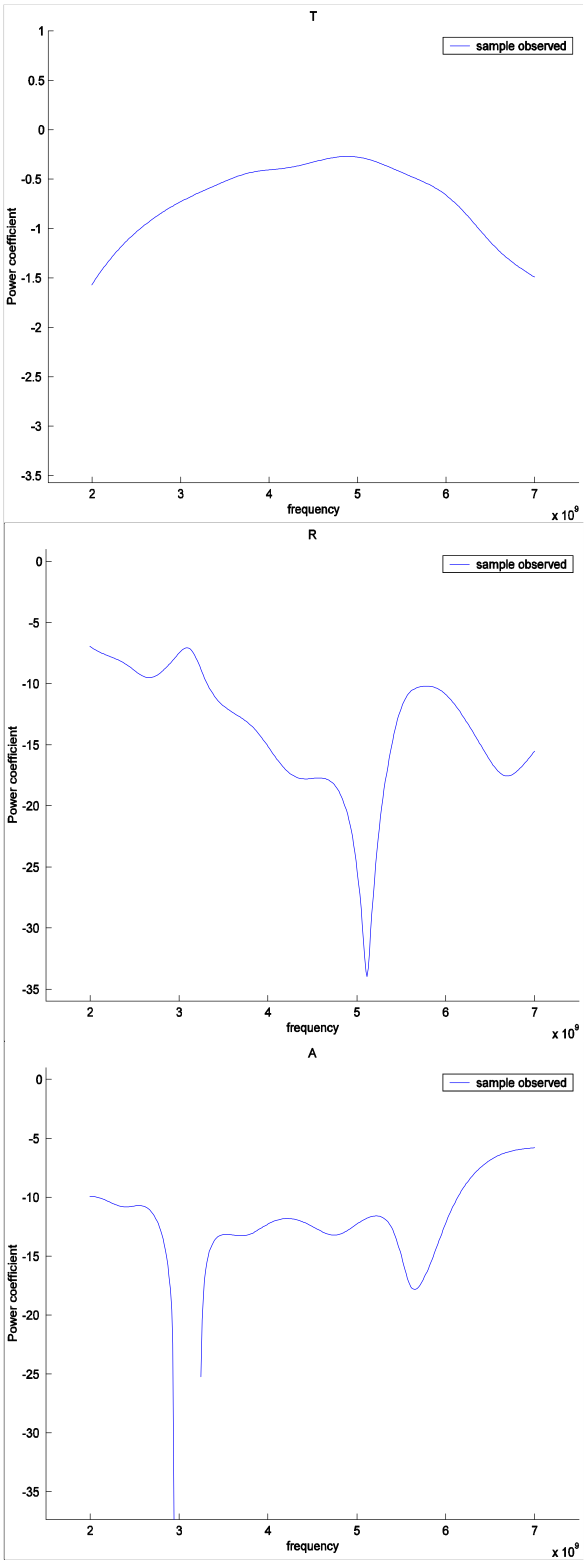

Figure 33: Paper Backed Wire Lath (for Stucco, Wire Side)

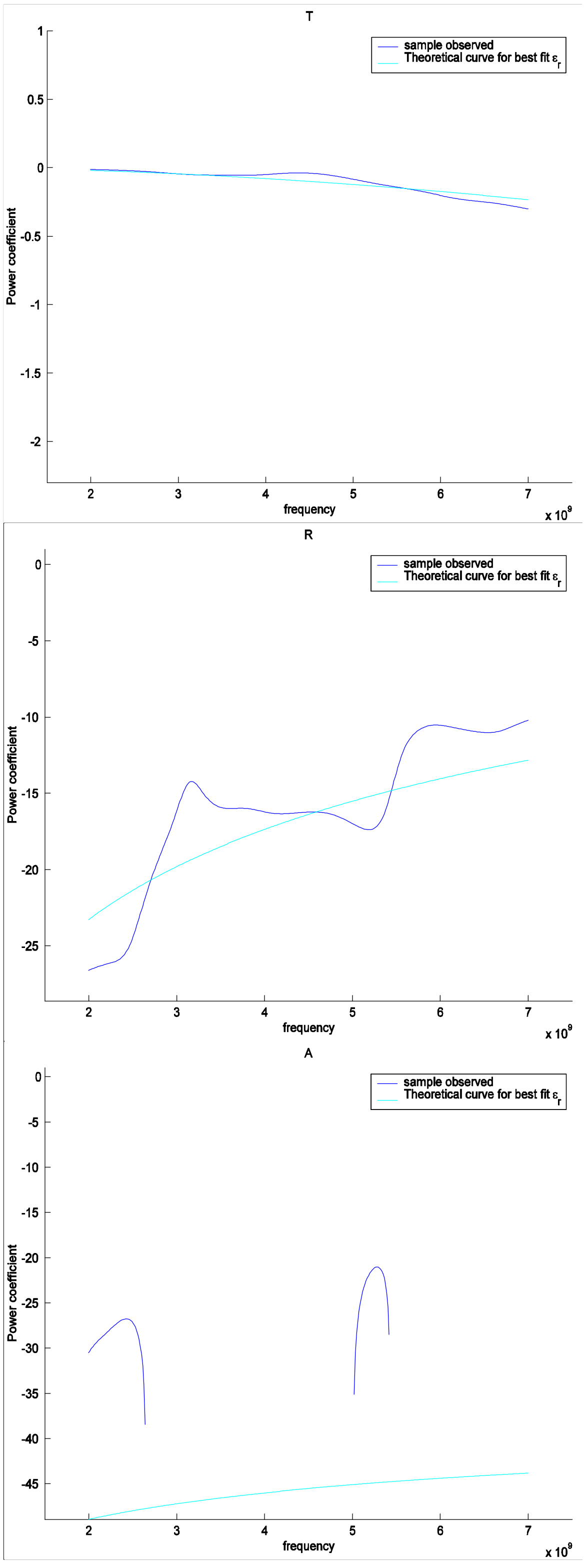

Figure 34: Linoleum (Back)

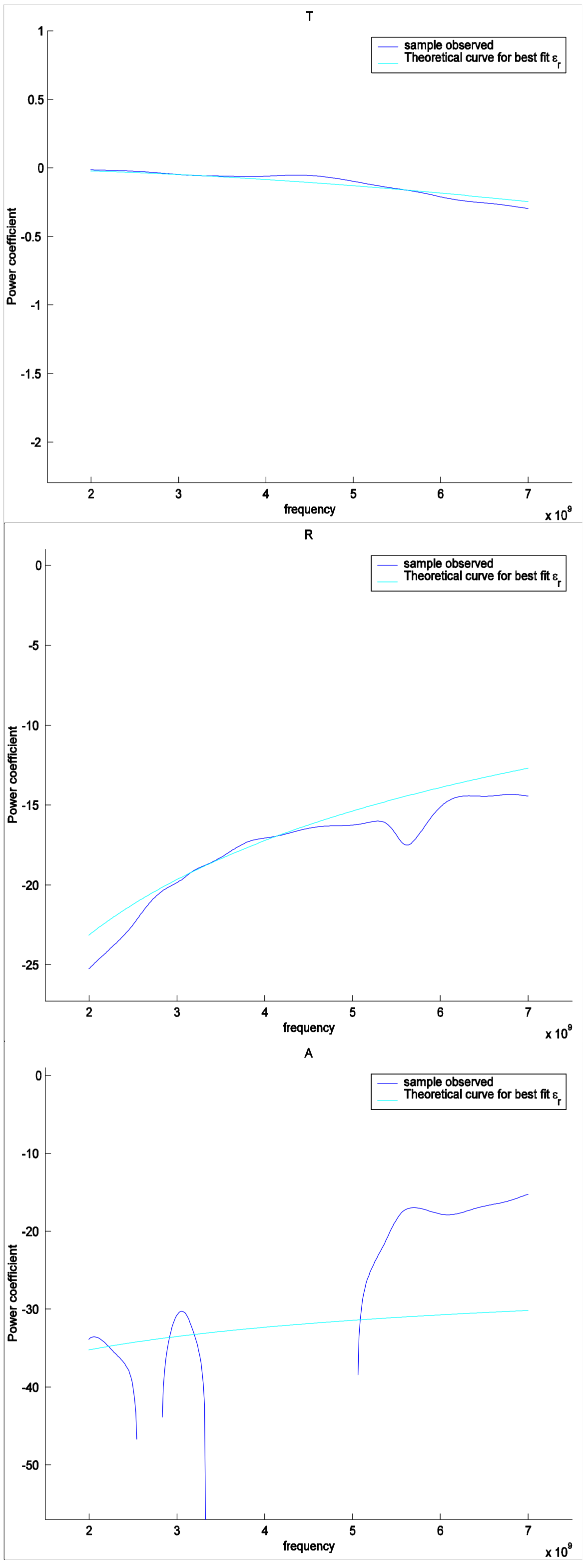

Figure 35: Linoleum (Front)

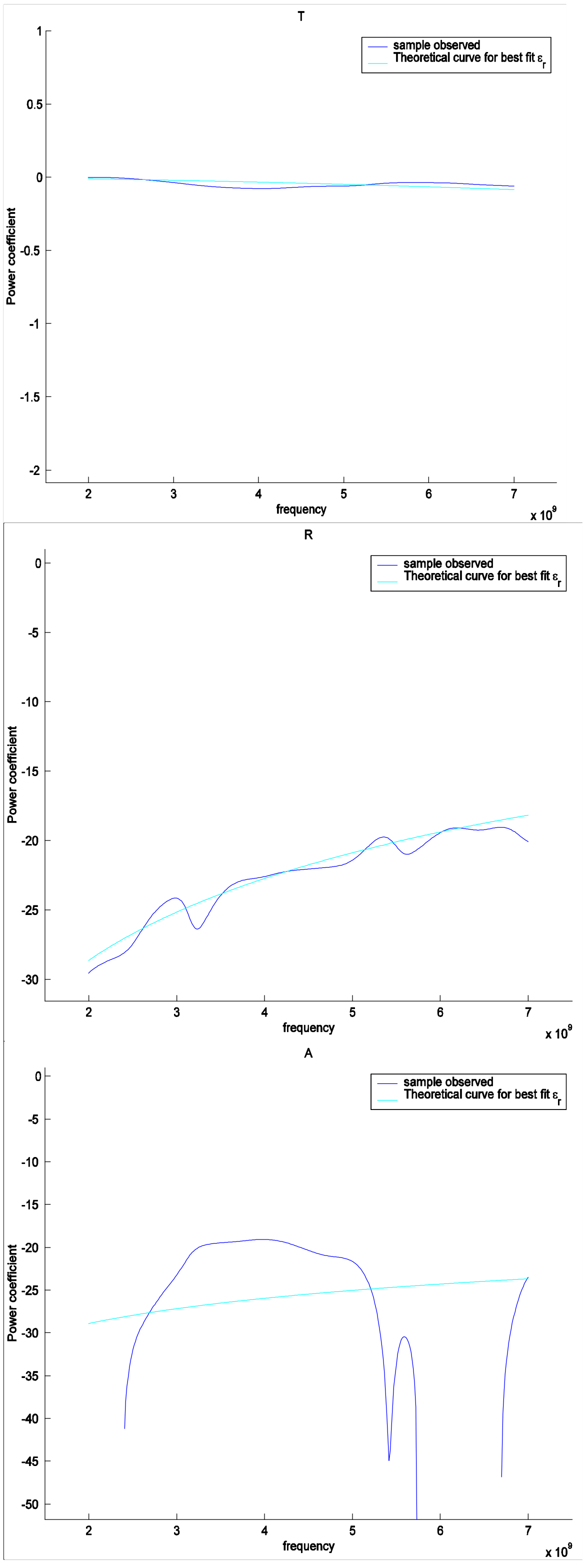

Figure 36: Light Cover (Front)

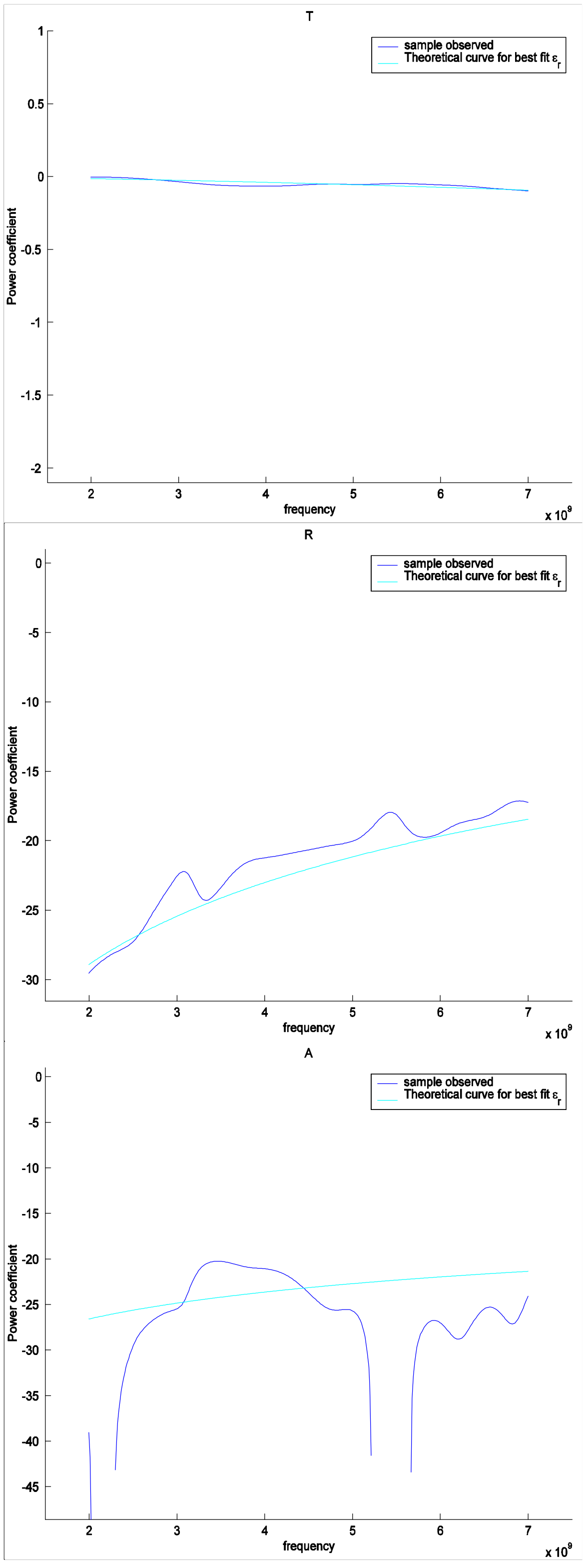

Figure 37: Light Cover (Back)

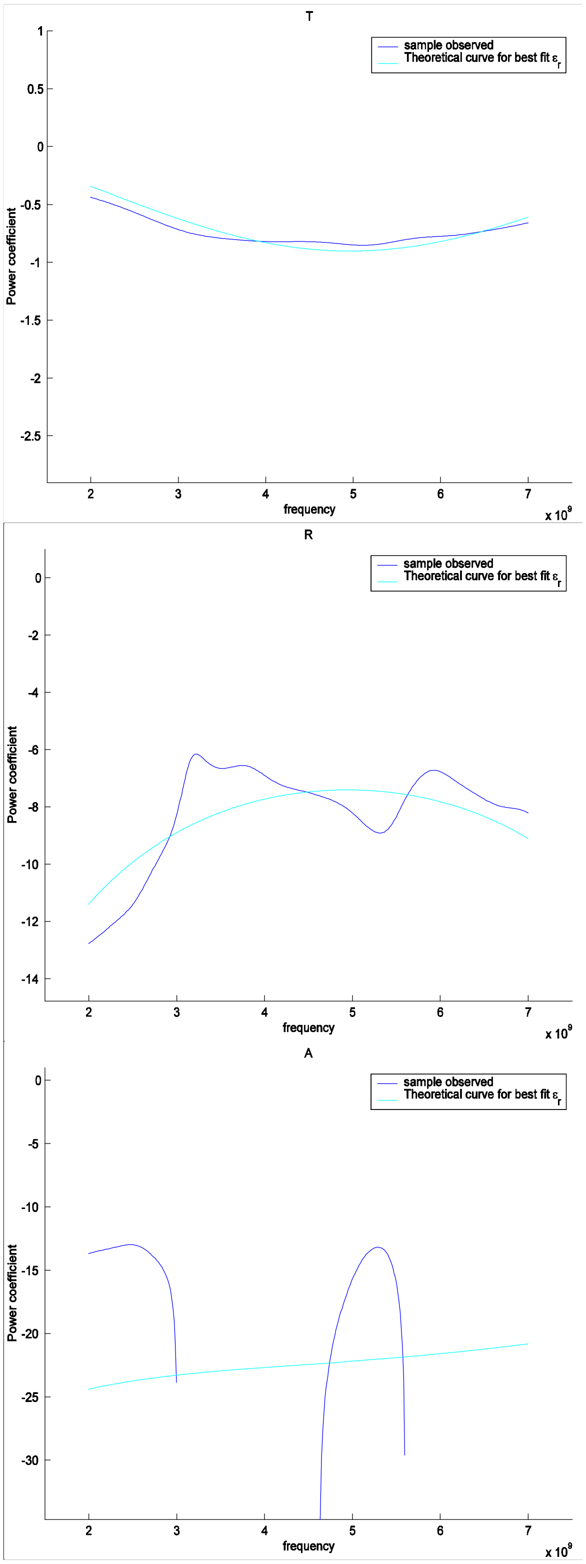

Figure 38: Drywall (8mm)

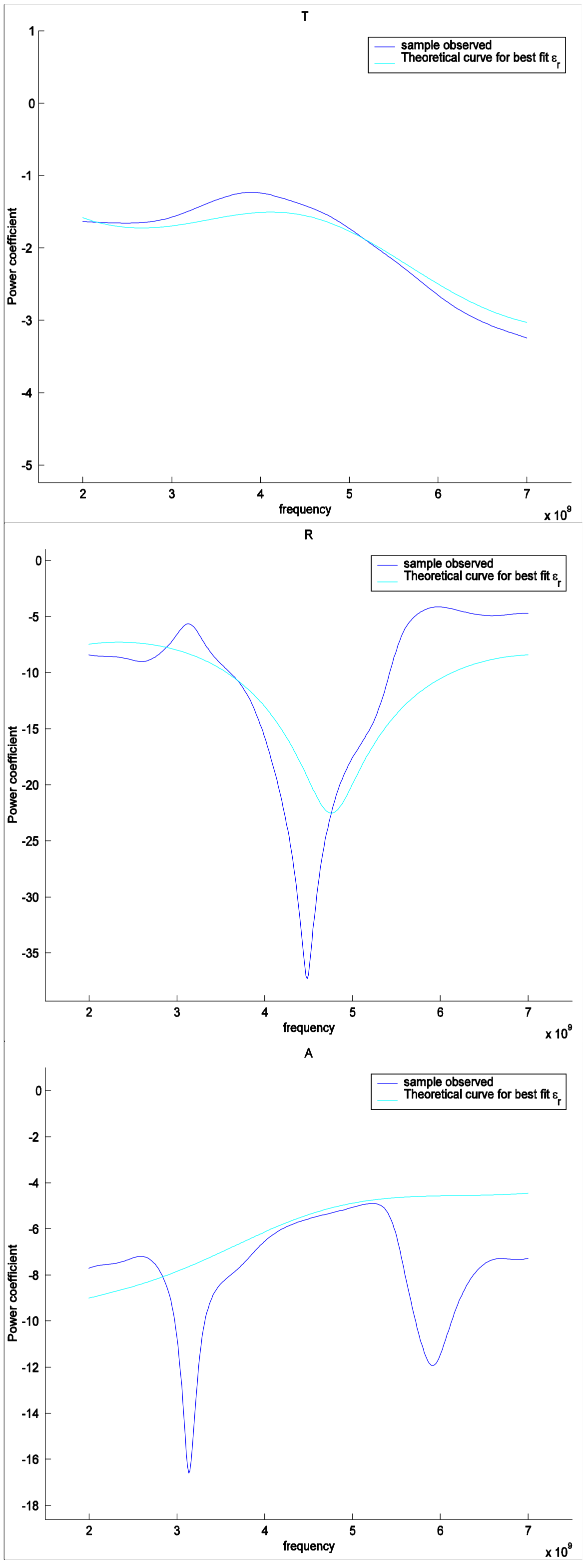

Figure 39: Particle Board

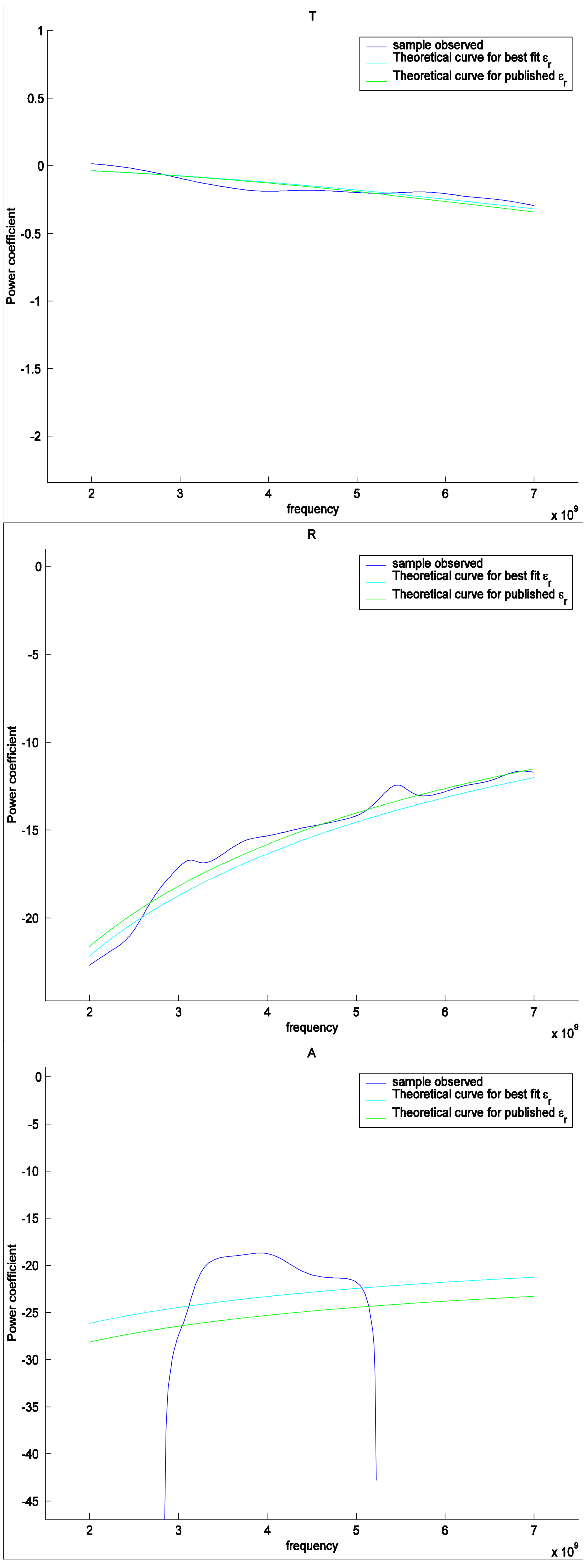

Figure 40: Plexiglass (2.5mm)

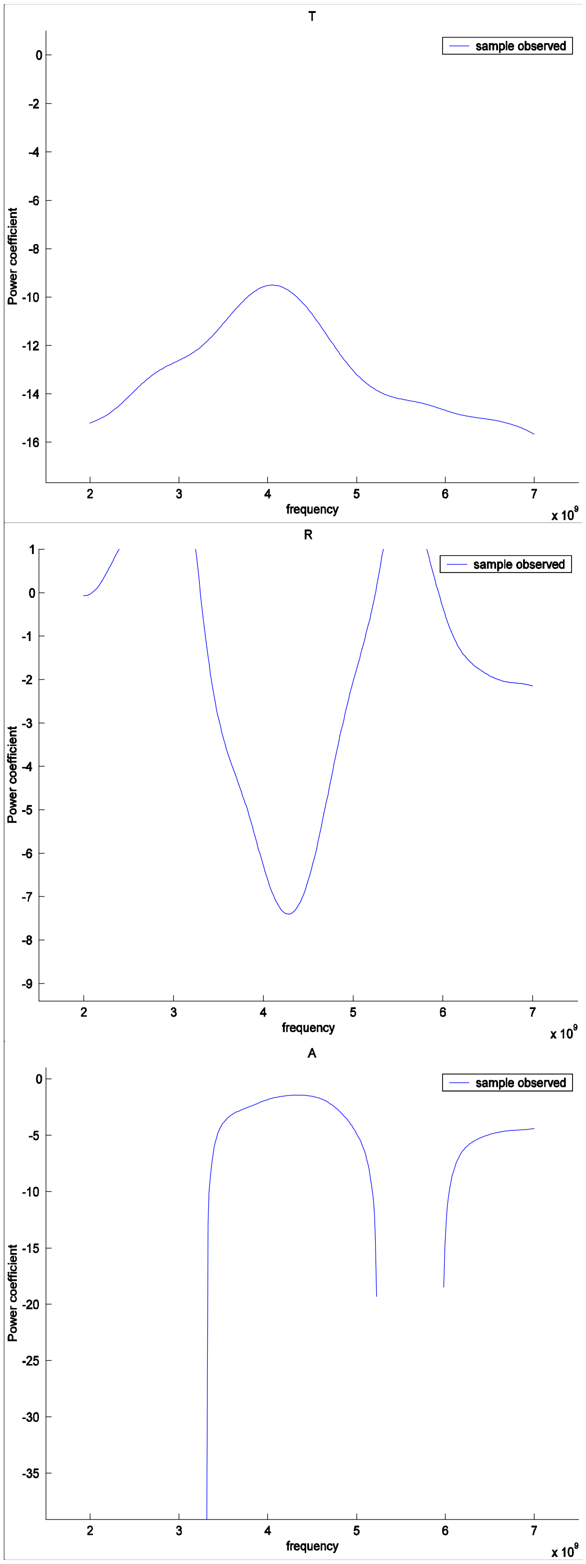

Figure 41: Stucco (Back)

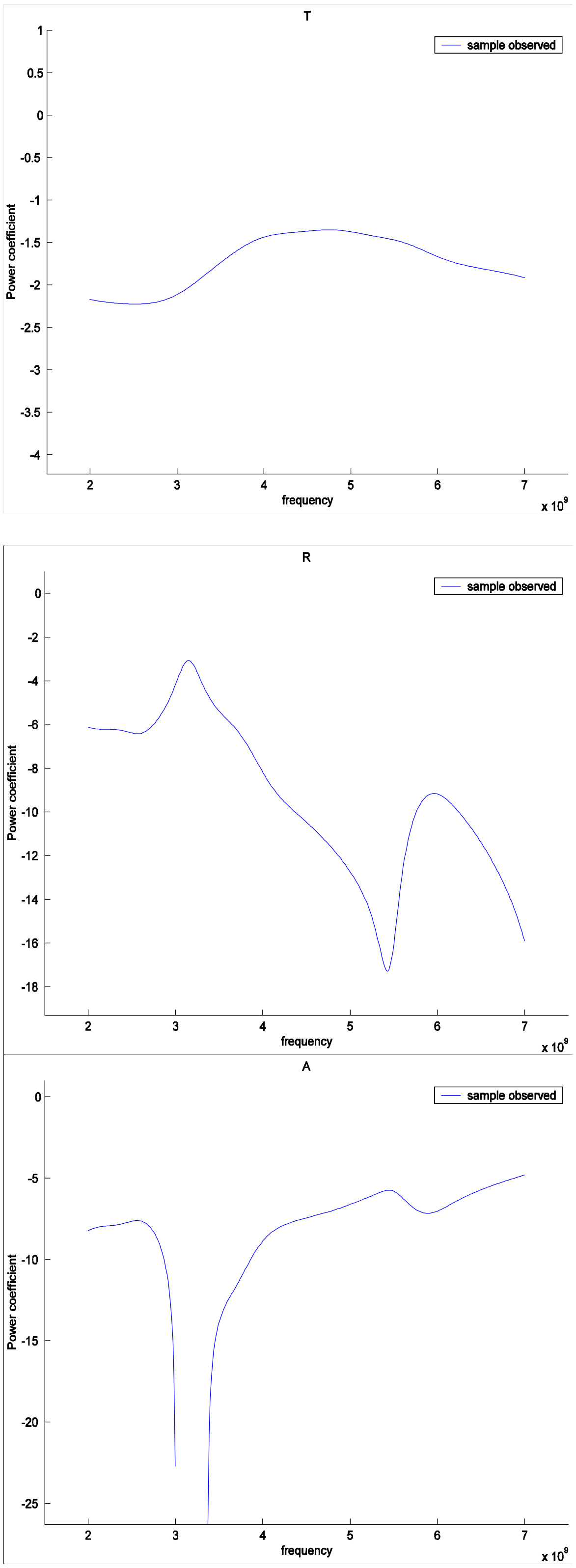

Figure 42: Bathroom Tile with Grout, Glued to 13mm Drywall

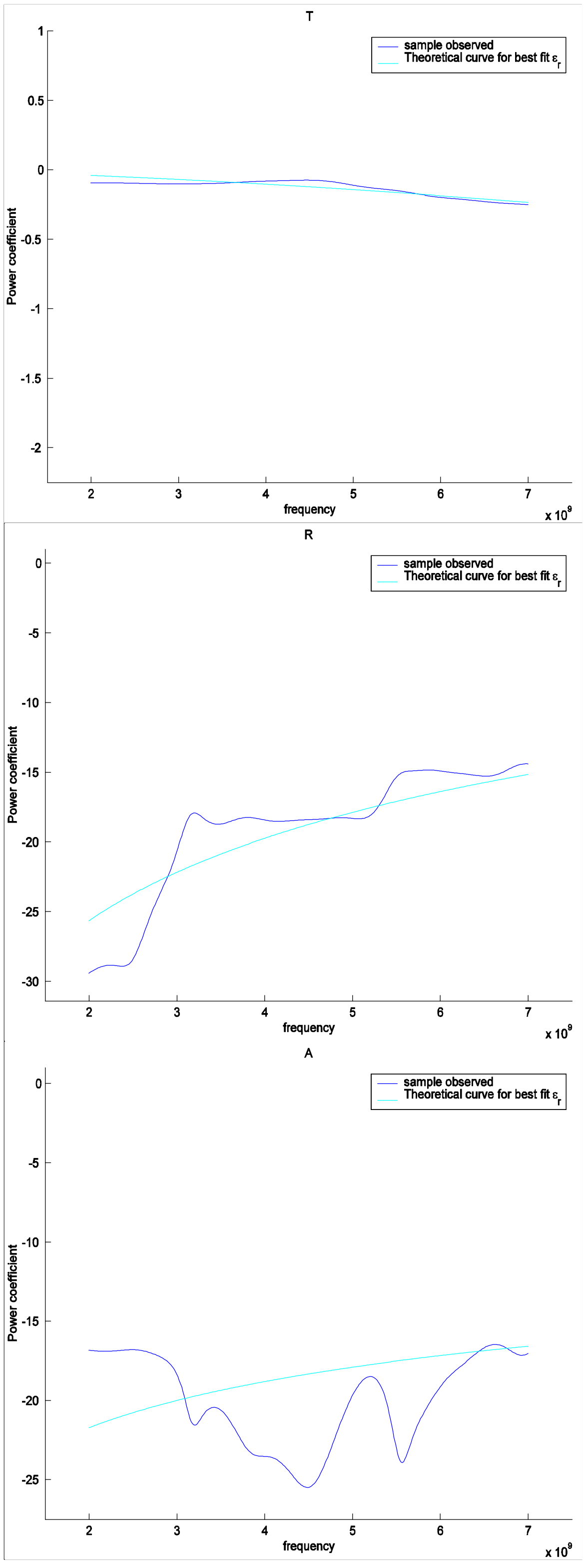

Figure 43: Tar Paper

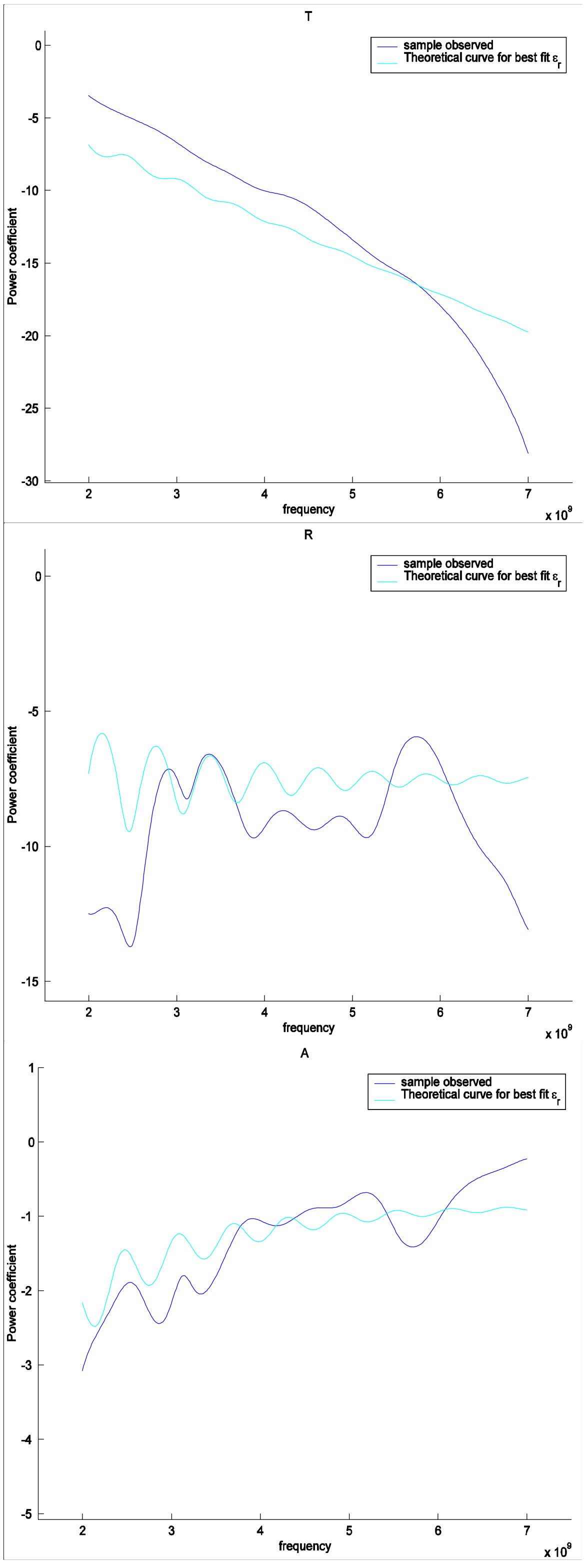

Figure 44: Wet Bricks

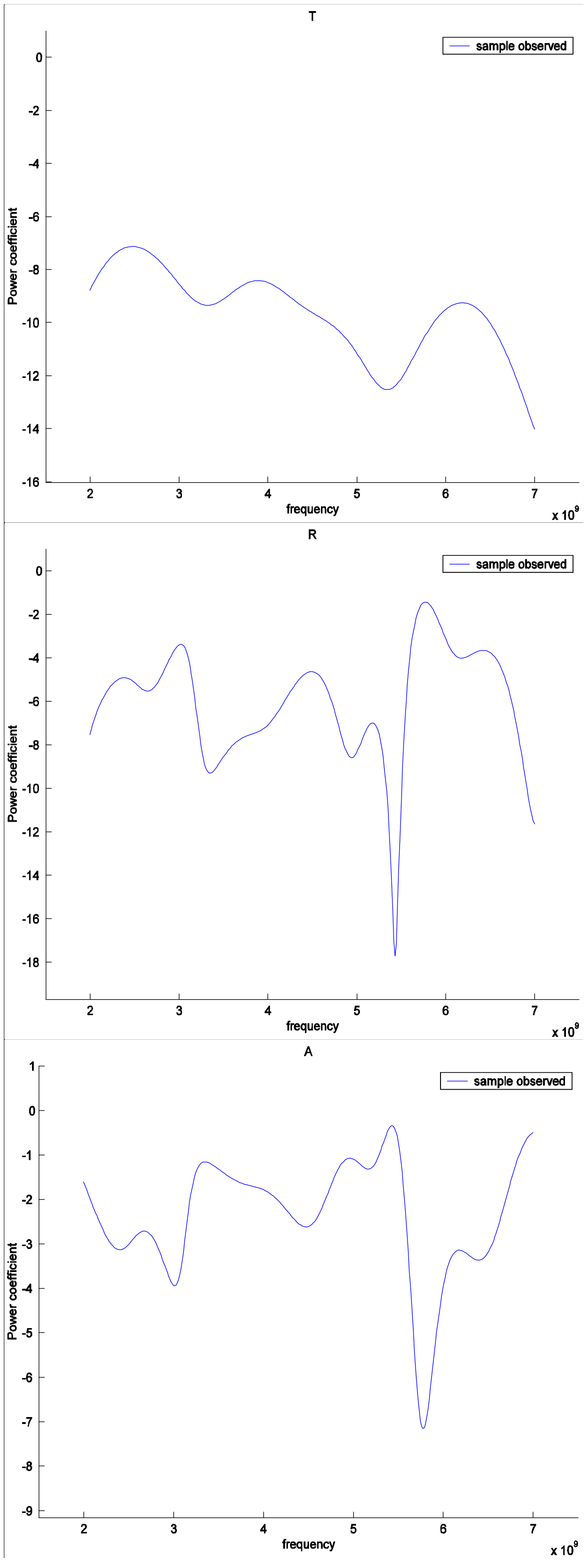

Figure 45: Wet Cinder Block

1. References

[1] O. Landrom, M. J. Feurstein and T. S. Rappaport, A Comparison of Theoretical and Empirical Reflection Coefficients for Typical Exterior Wall Surfaces in a Mobile Radio Environment, *IEEE Trans. Antennas Propagat.,* vol. 44, pp. 341-351, 1996.
[2] W. Honcharenko and H. L. Bertoni, Transmission and Reflection Characteristics at Concrete Block Walls in the UHF Bands Proposed for Future PCS, *IEEE Trans. Antennas Propagat.,* vol. 42, pp. 232-239, 1994.
[3] S. Kim, B. Bougerolles, and H. L. Bertoni, Transmission and Reflection Properties of Interior Walls, *Proc. IEEE ICUPC'94*, p. 124-128, 1994.
[4] G. Durgin, T.S. Rappaport, and H. Xu, 5.85-GHz Radio Path Loss and Penetration Loss Measurements in and Around Homes and Trees, *IEEE Commun. Let,* vol. 2, pp. 70-72, 1998.
[5] D. C. Cox, R. R. Murray, and A. W. Norris, 800-MHz Attenuation Measured in and Around Suburban Houses, *AT&T Bell Lab. Tech. J.,* vol. 63, pp. 921-953, 1984.
[6] J. F. Lafortune and M. Lecours, Measurement and Modeling of Propagation Losses in a Building at 900 MHz, *IEEE Trans Veh. Technol.,* vol. 39, pp. 101-108, 1990.
[7] S. Y. Seidel and T.S. Rappaport, 914 MHz Path Loss Prediction Models for Indoor Wireless Communications in Multifloored Buildings, *IEEE Trans. Antennas Propagat.,* vol. 40, pp. 207-217, 1992.
[8] Z. Abbas, R. D. Pollard, and R. W. Kelsall, Complex Permittivity Measurements at Ka-Band Using Rectangular Dielectric Waveguide, *IEEE Trans. Instr. Meas.,* vol. 50, pp. 1334-1342, 2001.
[9] J. Baker-Jarvis, E. J. Vanzura, and W. A. Kissick, Improved Technique for Determining Complex Permittivity with the Transmission/Reflection Method, *IEEE Trans. Microwave Theory Tech.,* vol. 38, pp 1096-1102, 1990
[10] J. Musil and F. Žácek, Microwave Measurements of Complex Permittivity by Free Space Methods and Their Applications, Elsevier, New York, 1986.
[11] D. Blackham, Free Space Characterization of Materials, Courtesy Test and Measurement Technical Support, Agilent Technologies.
[12] J. Matlacz and K. D. Palmer, Using Offset Parabolic Reflector Antennas for Free Space Material Measurement, *IEEE Trans. Instr. Meas.,* vol. 49, pp 862-866, 2000.
[13] V. V. Varadan, R. D. Hollinger, D. K. Ghodgaonkar and V. K. Varadan, Free-Space, Broadband Measurements of High-Temperature, Complex Dielectric Properties at Microwave

---

Frequencies, *IEEE Trans. Instr. Meas.,* vol. 40, pp 842-846, 2001.
[14] M. Nakhkash, Y. Huang, W. Al-Nuaimy, and M. T. C. Fang, An Improved Calibration Technique for Free-Space Measurement of Complex Permittivity, *IEEE Trans. Geoscience and Remote Sensing,* vol. 39, pp 453-455, 2001.
[15] I. Cuiñas and M. G. Sánchez, Building Material Characterization from Complex Transmissivity Measurements at 5.8 GHz, *IEEE Trans. Antennas Propagat.,* vol. 48, pp 1269-1271, 2000
[16] M. Sucher and J. Fox, *Handbook of Microwave Measurements*, Vol. 2, Polytechnic Press of the Polytechnic Institute of Brooklyn, New York, 1963.
[17] A. von Hippel, *Dielectrics and Waves,* Artech House, Boston, 1995.
[18] M. N. Asfar, J. R. Birch, and R. N. Clarke, The Measurement of the Properties of Materials, *Proc. IEEE,* vol. 74, 1986.
[19] J. R. Birch *et. al.,* An Intercomparison of Measurement Techniques for the Determination of the Dielectric Properties of Solids at Near Millimeter Wavelengths, *IEEE Trans. Micr. Theory and Tech.,* vol. 43, 1994.
[20] H. L. Bertoni, *Radio Propagation for Modern Wireless Systems*, Prentice Hall, New Jersey, 2000.
[21] Hewlett Packard Users Guide, HP8720D Network Analyzer, pg. 5-25.
[22]A. von Hippel (ed.), *Dielectric Materials and Applications,* Artech House, Boston, 1995.
[23] G. I. Torgovnikov, Dielectric Properties of Wood and Wood-based Materials, Springer-Verlag, Berlin, 1993.

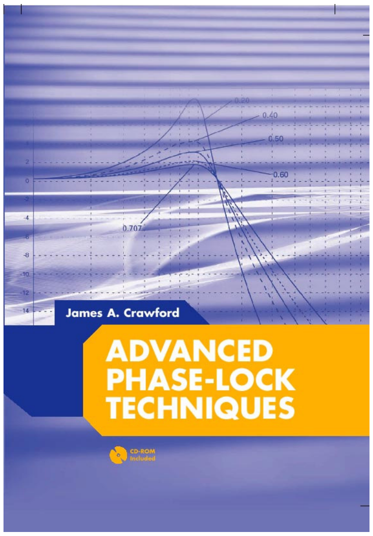

Advanced Phase-Lock Techniques

James A. Crawford

2008

Artech House

510 pages, 480 figures, 1200 equations
CD-ROM with all MATLAB scripts

ISBN-13: 978-1-59693-140-4
ISBN-10: 1-59693-140-X

Chapter	Brief Description	*Pages*
1	*Phase-Locked Systems—A High-Level Perspective* An expansive, multi-disciplined view of the PLL, its history, and its wide application.	26
2	*Design Notes* A compilation of design notes and formulas that are developed in details separately in the text. Includes an exhaustive list of closed-form results for the classic type-2 PLL, many of which have not been published before.	44
3	*Fundamental Limits* A detailed discussion of the many fundamental limits that PLL designers may have to be attentive to or else never achieve their lofty performance objectives, e.g., Paley-Wiener Criterion, Poisson Sum, Time-Bandwidth Product.	38
4	*Noise in PLL-Based Systems* An extensive look at noise, its sources, and its modeling in PLL systems. Includes special attention to $1/f$ noise, and the creation of custom noise sources that exhibit specific power spectral densities.	66
5	*System Performance* A detailed look at phase noise and clock-jitter, and their effects on system performance. Attention given to transmitters, receivers, and specific signaling waveforms like OFDM, M-QAM, M-PSK. Relationships between EVM and image suppression are presented for the first time. The effect of phase noise on channel capacity and channel cutoff rate are also developed.	48
6	*Fundamental Concepts for Continuous-Time Systems* A thorough examination of the classical continuous-time PLL up through 4th-order. The powerful Haggai constant phase-margin architecture is presented along with the type-3 PLL. Pseudo-continuous PLL systems (the most common PLL type in use today) are examined rigorously. Transient response calculation methods, 9 in total, are discussed in detail.	71
7	*Fundamental Concepts for Sampled-Data Control Systems* A thorough discussion of sampling effects in continuous-time systems is developed in terms of the z-transform, and closed-form results given through 4th-order.	32
8	*Fractional-N Frequency Synthesizers* A historic look at the fractional-N frequency synthesis method based on the U.S. patent record is first presented, followed by a thorough treatment of the concept based on Δ-Σ methods.	54
9	*Oscillators* An exhaustive look at oscillator fundamentals, configurations, and their use in PLL systems.	62
10	*Clock and Data Recovery* Bit synchronization and clock recovery are developed in rigorous terms and compared to the theoretical performance attainable as dictated by the Cramer-Rao bound.	52

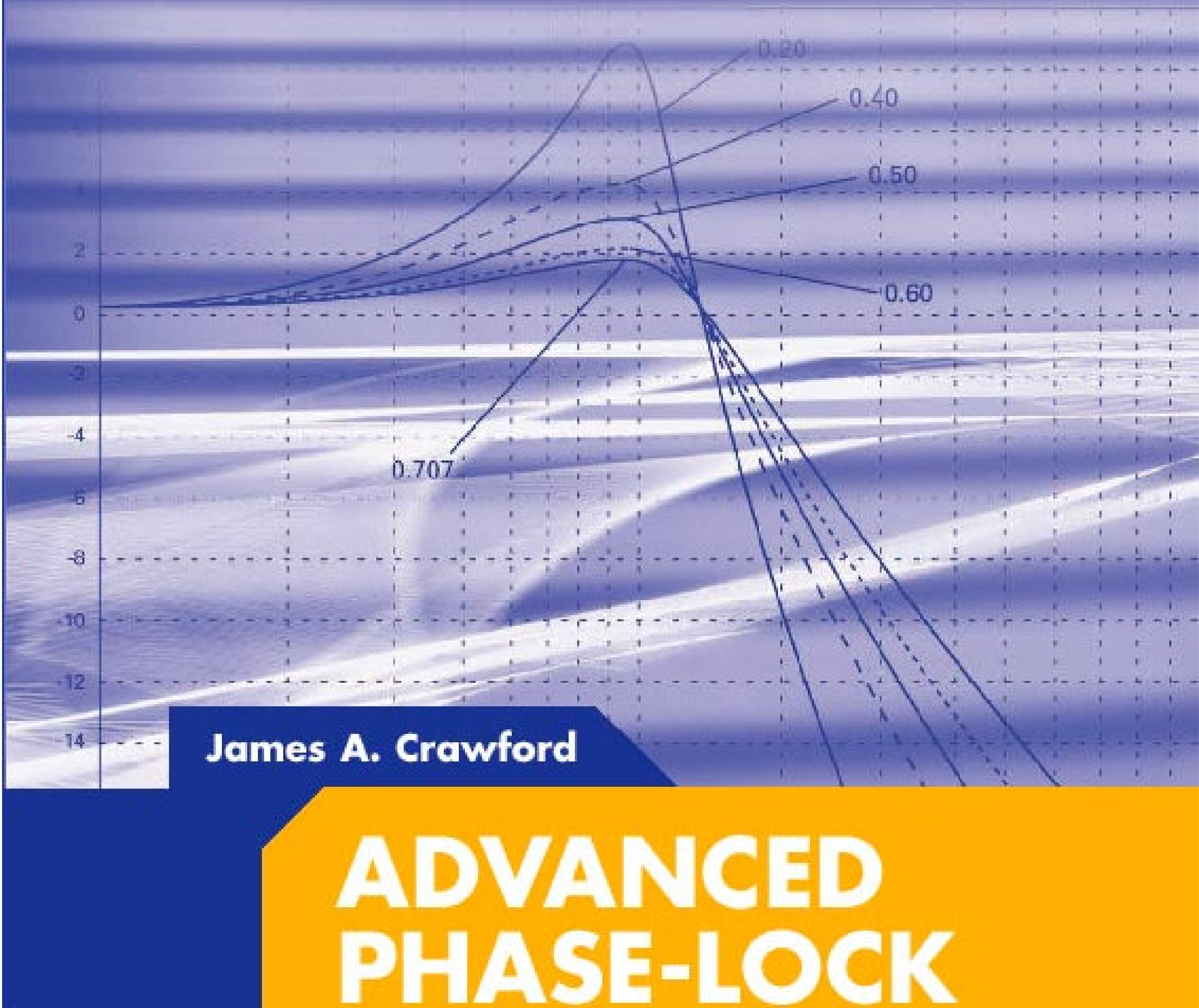

James A. Crawford

ADVANCED PHASE-LOCK TECHNIQUES

CD-ROM Included

Advanced Phase-Lock Techniques

James A. Crawford

ARTECH
HOUSE
BOSTON | LONDON
artechhouse.com

Library of Congress Cataloging-in-Publication Data
A catalog record for this book is available from the U.S. Library of Congress.

British Library Cataloguing in Publication Data
A catalogue record for this book is available from the British Library.

ISBN-13: 978-1-59693-140-4

Cover design by Yekaterina Ratner

685 Canton Street
Norwood, MA 02062

10 9 8 7 6 5 4 3 2 1

are described further for the ideal type-2 PLL in Table 1-1. The feedback divider is normally present only in frequency synthesis applications, and is therefore shown as an optional element in this figure.

PLLs are most frequently discussed in the context of continuous-time and Laplace transforms. A clear distinction is made in this text between continuous-time and discrete-time (i.e., sampled) PLLs because the analysis methods are, rigorously speaking, related but different. A brief introduction to continuous-time PLLs is provided in this section with more extensive details provided in Chapter 6.

PLL type and *PLL order* are two technical terms that are frequently used interchangeably even though they represent distinctly different quantities. PLL *type* refers to the number of ideal poles (or integrators) within the linear system. A voltage-controlled oscillator (VCO) is an ideal integrator of phase, for example. PLL *order* refers to the order of the characteristic equation polynomial for the linear system (e.g., denominator portion of (1.4)). The loop-order must always be greater than or equal to the loop-type. Type-2 third- and fourth-order PLLs are discussed in Chapter 6, as well as a type-3 PLL, for example.

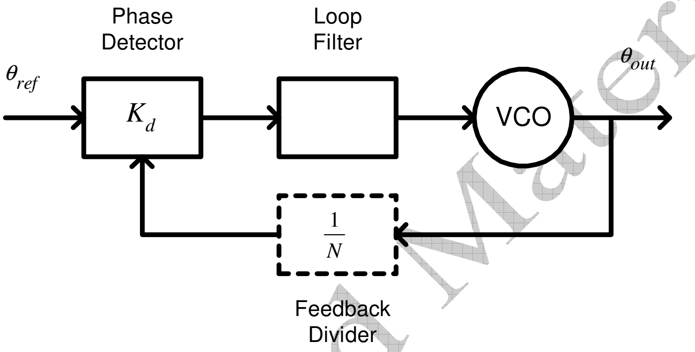

Figure 1-2 Basic PLL structure exhibiting the basic functional ingredients.

Table 1-1
Basic Constitutive Elements for a Type-2 Second-Order PLL

Block Name	Laplace Transfer Function	Description
Phase Detector	K_d, V/rad	Phase error metric that outputs a voltage that is proportional to the phase error existing between its input θ_{ref} and the feedback phase θ_{out}/N. Charge-pump phase detectors output a current rather than a voltage, in which case K_d has units of A/rad.
Loop Filter	$\frac{1+s\tau_2}{s\tau_1}$	Also called the lead-lag network, it contains one ideal pole and one finite zero.
VCO	$\frac{K_v}{s}$	The voltage-controlled oscillator (VCO) is an ideal integrator of phase. K_v normally has units of rad/s/V.
Feedback Divider	$1/N$	A digital divider that is represented by a continuous divider of phase in the continuous-time description.

The type-2 second-order PLL is arguably the workhorse even for modern PLL designs. This PLL is characterized by (i) its natural frequency ω_n (rad/s) and (ii) its damping factor ζ. These terms are used extensively throughout the text, including the examples used in this chapter. These terms are separately discussed later in Sections 6.3.1 and 6.3.2. The role of these parameters in shaping the time- and frequency-domain behavior of this PLL is captured in the extensive list of formula provided in Section 2.1. In the continuous-time-domain, the type-2 second-order PLL[3] open-loop gain function is given by

---

[3] See Section 6.2.

$$G_{OL}(s)=\left(\frac{\omega_n}{s}\right)^2\frac{1+s\tau_2}{s\tau_1} \quad (1.1)$$

and the key loop parameters are given by

$$\omega_n=\sqrt{\frac{K_d K_v}{N\tau_1}} \quad (1.2)$$

$$\zeta=\frac{1}{2}\omega_n\tau_2 \quad (1.3)$$

The time constants τ_1 and τ_2 are associated with the loop filter's R and C values as developed in Chapter 6. The closed-loop transfer function associated with this PLL is given by the classical result

$$H_1(s)=\frac{1}{N}\frac{\theta_{out}(s)}{\theta_{ref}(s)}=\frac{\omega_n^2\left(1+\frac{2\zeta}{\omega_n}s\right)}{s^2+2\zeta\omega_n s+\omega_n^2} \quad (1.4)$$

The transfer function between the synthesizer output phase noise and the VCO self-noise is given by $H_2(s)$ where

$$H_2(s)=1-H_1(s) \quad (1.5)$$

A convenient frequency-domain description of the open-loop gain function is provided in Figure 1-3. The frequency break-points called out in this figure and the next two appear frequently in PLL work and are worth committing to memory. The unity-gain radian frequency is denoted by ω_u in this figure and is given by

$$\omega_u=\omega_n\sqrt{2\zeta^2+\sqrt{4\zeta^4+1}} \quad (1.6)$$

A convenient approximation for the unity-gain frequency (1.6) is given by $\omega_u \cong 2\zeta\omega_n$. This result is accurate to within 10% for $\zeta \geq 0.704$.

The $H_1(s)$ transfer function determines how phase noise sources appearing at the PLL input are conveyed to the PLL output and a number of other important quantities. Normally, the input phase noise spectrum is assumed to be spectrally flat resulting in the output spectrum due to the reference noise being shaped entirely by $|H_1(s)|^2$. A representative plot of $|H_1|^2$ is shown in Figure 1-4. The key frequencies in the figure are the frequency of maximum gain, the zero dB gain frequency, and the –3 dB gain frequency which are given respectively by

$$F_{Pk}=\frac{1}{2\pi}\frac{\omega_n}{2\zeta}\sqrt{\sqrt{1+8\zeta^2}-1}\ \text{Hz} \quad (1.7)$$

$$F_{0dB}=\frac{1}{2\pi}\sqrt{2}\omega_n\ \text{Hz} \quad (1.8)$$

$$F_{3dB}=\frac{\omega_n}{2\pi}\sqrt{1+2\zeta^2+2\sqrt{\zeta^4+\zeta^2+\frac{1}{2}}}\ \text{Hz} \quad (1.9)$$

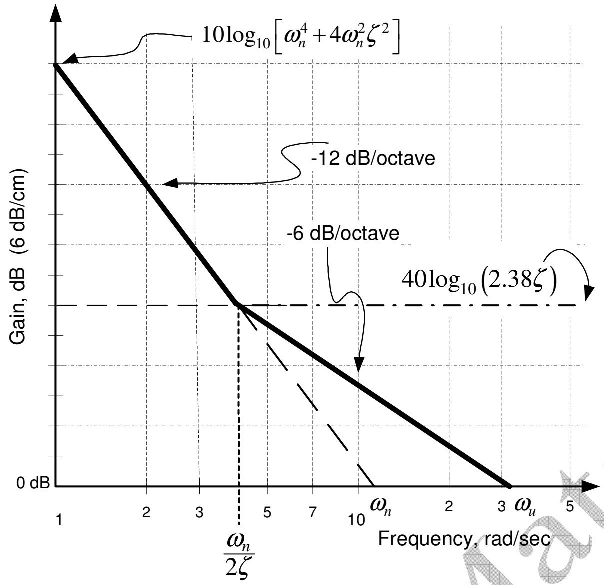

Figure 1-3 Open-loop gain approximations for classic continuous-time type-2 PLL.

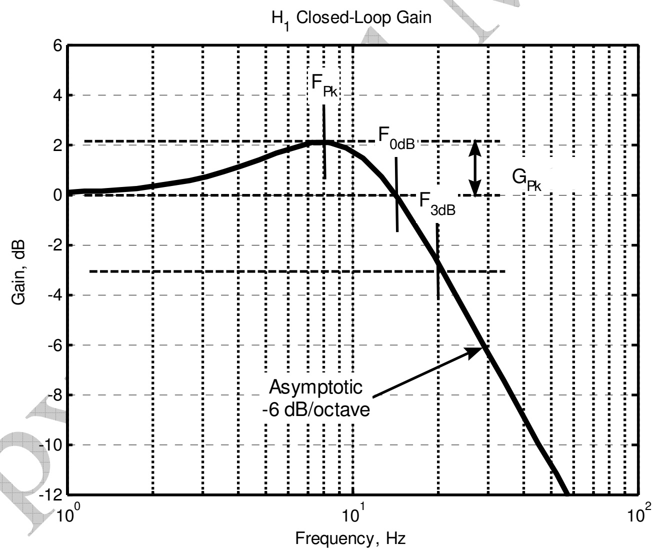

Figure 1-4 Closed-loop gain $H_1(f)$ for type-2 second-order PLL[4] from (1.4).

The amount of *gain-peaking* that occurs at frequency F_{pk} is given by

$$G_{Pk} = 10\log_{10}\left(\frac{8\zeta^4}{8\zeta^4 - 4\zeta^2 - 1 + \sqrt{1+8\zeta^2}}\right)\text{dB} \qquad (1.10)$$

For situations where the close-in phase noise spectrum is dominated by reference-related phase noise, the amount of gain-peaking can be directly used to infer the loop's damping factor from (1.10), and the

---

[4] Book CD:\Ch1\u14033_figequs.m, $\zeta = 0.707$, $\omega_n = 2\pi\,10$ Hz.

loop's natural frequency from (1.7). Normally, the close-in (i.e., radian offset frequencies less than $\omega_n/2\zeta$) phase noise performance of a frequency synthesizer is entirely dominated by reference-related phase noise since the VCO phase noise generally increases 6 dB/octave with decreasing offset frequency[5] whereas the open-loop gain function exhibits a 12 dB/octave increase in this same frequency range.

VCO-related phase noise is attenuated by the $H_2(s)$ transfer function (1.5) at the PLL's output for offset frequencies less than approximately ω_n. At larger offset frequencies, $H_2(s)$ is insufficient to suppress VCO-related phase noise at the PLL's output. Consequently, the PLL's output phase noise spectrum is normally dominated by the VCO self-noise phase noise spectrum for the larger frequency offsets. The key frequency offsets and relevant $H_2(s)$ gains are shown in Figure 1-5 and given in Table 1-2.

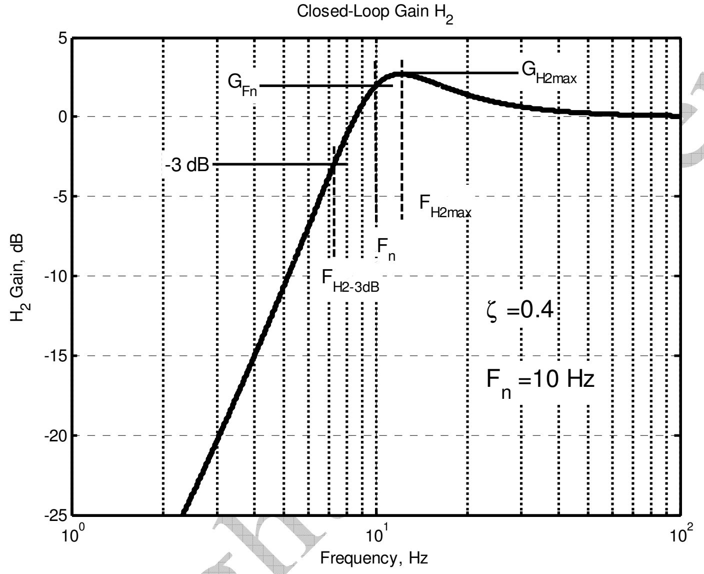

Figure 1-5 Closed-loop gain[6] H_2 and key frequencies for the classic continuous-time type-2 PLL.

Table 1-2

Key Frequencies Associated with $H_2(s)$ for the Ideal Type-2 PLL

Frequency, Hz	**Associated H_2 Gain, dB**	**Constraints on ζ**
$1/2\pi$	$G_{H_2\_1rad/s} = -10\log_{10}\left[\omega_n^4 + \omega_n^2\left(4\zeta^2 - 2\right) + 1\right]$	—
$F_{H_2-3dB} = \dfrac{\omega_n}{2\pi}\left[2\zeta^2 - 1 + \sqrt{2 - 4\zeta^2 + 4\zeta^4}\right]^{1/2}$	–3	—
$F_{H_2\_0dB} = \dfrac{1}{2\pi}\dfrac{\omega_n}{\sqrt{2 - 4\zeta^2}}$	0	$\zeta < \dfrac{\sqrt{2}}{2}$
$F_n = \omega_n / 2\pi$	$G_{H_2\_\omega_n} = -10\log_{10}\left(4\zeta^2\right)$	—
$F_{H_2\_\max} = \dfrac{1}{2\pi}\dfrac{\omega_n}{\sqrt{1 - 2\zeta^2}}$	$G_{H_2\_\max} = -10\log_{10}\left(4\zeta^2 - 4\zeta^4\right)$	$\zeta < \dfrac{\sqrt{2}}{2}$

---

[5] Leeson's model in Section 9.5.1; Haggai oscillator model in Section 9.5.2.

[6] Book CD:\Ch1\u14035_h2.m.

Assuming that the noise samples have equal variances and are uncorrelated, $R = \sigma_n^2 I$ where I is the $K \times K$ identity matrix. In order to maximize (1.43) with respect to θ, a necessary condition is that the derivative of (1.43) with respect to θ be zero, or equivalently

$$\begin{aligned}\frac{\partial L}{\partial \theta} &= \frac{\partial}{\partial \theta}\sum_k \left[r_k - A\cos\left(\omega_o t_k + \theta\right)\right]^2 = 0 \\ &= \sum_k 2\left[r_k - A\cos\left(\omega_o t_k + \theta\right)\right] A\sin\left(\omega_o t_k + \theta\right) = 0\end{aligned} \tag{1.44}$$

Simplifying this result further and discarding the double-frequency terms that appear, the maximum-likelihood estimate for θ is that value that satisfies the constraint

$$\overline{\sum_k r_k \sin\left(\omega_o t_k + \hat{\theta}\right)} = 0 \tag{1.45}$$

The top line indicates that double-frequency terms are to be filtered out and discarded. This result is equivalent to the minimum-variance estimator just derived in (1.40).

Under the assumed linear Gaussian conditions, the minimum-variance (MV) and maximum-likelihood (ML) estimators take the same form when implemented with a PLL. Both algorithms seek to reduce any quadrature error between the estimate and the observation data to zero.

1.4.3 PLL as a Maximum A Posteriori (MAP)-Based Estimator

The *MAP estimator* is used for the estimation of random parameters whereas the maximum-likelihood (ML) form is generally associated with the estimation of deterministic parameters. From *Bayes rule* for an observation *z*, the a posteriori probability density is given by

$$p(\theta|z) = \frac{p(z|\theta)p(\theta)}{p(z)} \tag{1.46}$$

and this can be re-written in the logarithmic form as

$$\log_e\left[p(\theta|z)\right] = \log_e\left[p(z|\theta)\right] + \log_e\left[p(\theta)\right] - \log_e\left[p(z)\right] \tag{1.47}$$

This log-probability may be maximized by setting the derivative with respect to θ to zero thereby creating the necessary condition that[27]

$$\frac{d}{d\theta}\left\{\log_e\left[p(z|\theta)\right] + \log_e\left[p(\theta)\right]\right\}_{\theta = \hat{\theta}_{MAP}} = 0 \tag{1.48}$$

If the density $p(\theta)$ is not known, the second term in (1.48) is normally discarded (set to zero) which degenerates naturally to the maximum-likelihood form as

$$\frac{d}{d\theta}\left\{\log_e\left[p(z|\theta)\right]\right\}_{\theta = \hat{\theta}_{ML}} = 0 \tag{1.49}$$

---

[27] [15] Section 6.2.1, [17] Section 2.4.1, [18] Section 5.4, and [22].

Time of Peak Phase-Error with Frequency-Step Applied

$$T_{fstep} = \frac{1}{\omega_n\sqrt{1-\zeta^2}}\tan^{-1}\left(\frac{\sqrt{1-\zeta^2}}{\zeta}\right) \tag{2.29}$$

Note.[1] See Figure 2-19 and Figure 2-20.

Time of Peak Phase-Error with Phase-Step Applied

$$T_{\theta step} = \frac{1}{\omega_n\sqrt{1-\zeta^2}}\tan^{-1}\left(2\zeta\sqrt{1-\zeta^2},2\zeta^2-1\right) = \frac{2}{\omega_n\sqrt{1-\zeta^2}}\tan^{-1}\left(\frac{\sqrt{1-\zeta^2}}{\zeta}\right) \tag{2.30}$$

See Figure 2-19 and Figure 2-20.

Time of Peak Frequency-Error with Phase-Step Applied

$$T_{pk} = \frac{1}{\omega_n\sqrt{1-\zeta^2}}\begin{cases}\zeta \le \frac{1}{2}: & \theta_u \\ \zeta > \frac{1}{2}: & \theta_u + \pi\end{cases} \tag{2.31}$$

$$\text{with } \theta_u = \tan^{-1}\left[\left(1-4\zeta^2\right)\sqrt{1-\zeta^2},3\zeta-4\zeta^3\right] \tag{2.32}$$

See Figure 2-21 and Figure 2-22.

T_{pk} corresponds to the *first point* in time where $\mathrm{d}f_o/\mathrm{d}t = 0$.

Maximum Frequency-Error with Phase-Step Applied

Use (2.31) in (2.28). (2.33)

Time of Peak Frequency-Error with Frequency-Step Applied

$$T_{pk} = \frac{2}{\omega_n\sqrt{1-\zeta^2}}\tan^{-1}\left(\frac{\sqrt{1-\zeta^2}}{\zeta}\right) \tag{2.34}$$

% Transient Frequency Overshoot for Frequency-Step Applied

$$OS_{\%} = \left[\cos\left(\sqrt{1-\zeta^2}\,\omega_n T_{pk}\right) - \frac{\zeta}{\sqrt{1-\zeta^2}}\sin\left(\sqrt{1-\zeta^2}\,\omega_n T_{pk}\right)\right]e^{-\zeta\omega_n T_{pk}} \times 100\% \tag{2.35}$$

$$T_{pk} = \frac{2}{\omega_n\sqrt{1-\zeta^2}}\tan^{-1}\left(\frac{\sqrt{1-\zeta^2}}{\zeta}\right) \tag{2.36}$$

Note.[2] See Figure 2-23 and Figure 2-24.

Linear Hold-In Range with Frequency-Step Applied (Without Cycle-Slip)

$$\Delta F_{\max} = \omega_n \exp\left[\frac{\zeta}{\sqrt{1-\zeta^2}}\tan^{-1}\left(\frac{\sqrt{1-\zeta^2}}{\zeta}\right)\right] \text{ Hz} \tag{2.37}$$

See Figure 2-25.

Linear Settling Time with Frequency-Step Applied (Without Cycle-Slip) (Approx.)

$$T_{Lock} \le \frac{1}{\zeta\omega_n}\log_e\left(\frac{\Delta F}{\delta F}\frac{1}{\sqrt{1-\zeta^2}}\right) \text{ sec} \tag{2.38}$$

for applied frequency-step of ΔF and residual δF remaining at lock

See Figure 2-26.

---

[1] The peak occurrence time is precisely one-half that given by (2.34).

[2] See Figure 2-24 for time of occurrence T_{pk} for peak overshoot/undershoot with $\omega_n = 2\pi$. Amount of overshoot/undershoot in percent provided in Figure 2-23.

2.3.2.2 Second-Order Gear Result for $H_1(z)$ for Ideal Type-2 PLL

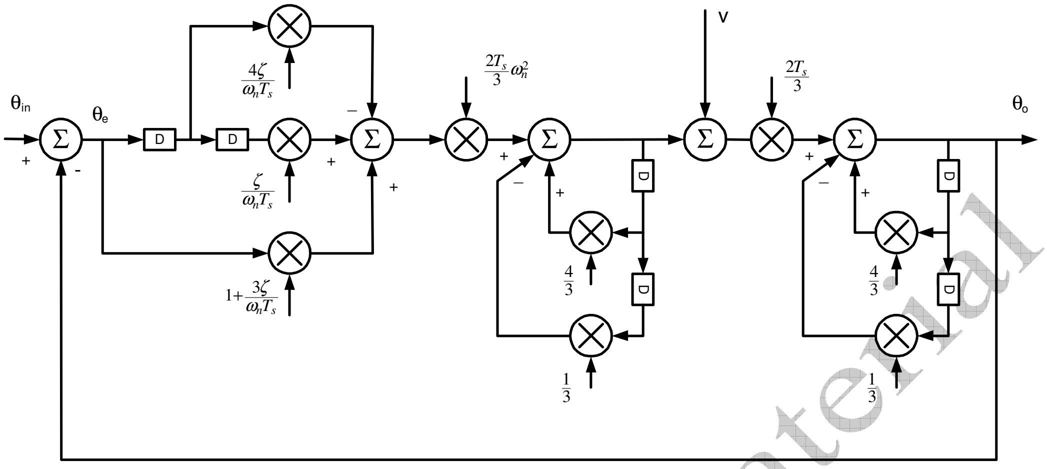

Figure 2-32 Second-order Gear redesign of $H_1(s)$ (2.4).

$$G_{OL}(z)=\left(\frac{2\omega_n T_s}{3}\right)^2 \frac{1+\frac{3\zeta}{\omega_n T_s}\left(1-\frac{4}{3}z^{-1}+\frac{1}{3}z^{-2}\right)}{\left(1-\frac{4}{3}z^{-1}+\frac{1}{3}z^{-2}\right)^2} \tag{2.52}$$

$$\theta_o(k)=\frac{1}{D}\left[\sum_{n=0}^{2}a_n\theta_{in}(k-n)+\sum_{n=0}^{2}b_n v(k-n)+\sum_{n=1}^{4}c_n\theta_o(k-n)\right] \tag{2.53}$$

$$\begin{aligned} a_0 &= 1+\frac{3\zeta}{\omega_n T_s} \\ a_1 &= -\frac{4\zeta}{\omega_n T_s} \\ a_2 &= \frac{\zeta}{\omega_n T_s} \end{aligned} \tag{2.54}$$

$$\begin{aligned} b_0 &= \frac{3}{2\omega_n^2 T_s} \\ b_1 &= -\frac{2}{\omega_n^2 T_s} \\ b_2 &= \frac{1}{2\omega_n^2 T_s} \end{aligned} \tag{2.55}$$

$$\begin{aligned} c_1 &= \frac{6}{(\omega_n T_s)^2}+\frac{4\zeta}{\omega_n T_s} \\ c_2 &= -\frac{11}{2(\omega_n T_s)^2}-\frac{\zeta}{\omega_n T_s} \\ c_3 &= \frac{2}{(\omega_n T_s)^2} \\ c_4 &= -\frac{1}{(2\omega_n T_s)^2} \end{aligned} \tag{2.56}$$

$$D=1+\frac{3\zeta}{\omega_n T_s}+\left(\frac{3}{2\omega_n T_s}\right)^2 \tag{2.57}$$

2.3.3 Higher-Order Differentiation Formulas

In cases where a precision first-order time-derivative $f(x_{n+1})$ must be computed from an equally spaced sample sequence, higher-order formulas may be helpful.[8] Several of these are provided here in Table 2-2. The uniform time between samples is represented by T_s.

---

[8] Precisions compared in Book CD:\Ch2\u14028_diff_forms.m.

2.5.5 64-QAM Symbol Error Rate

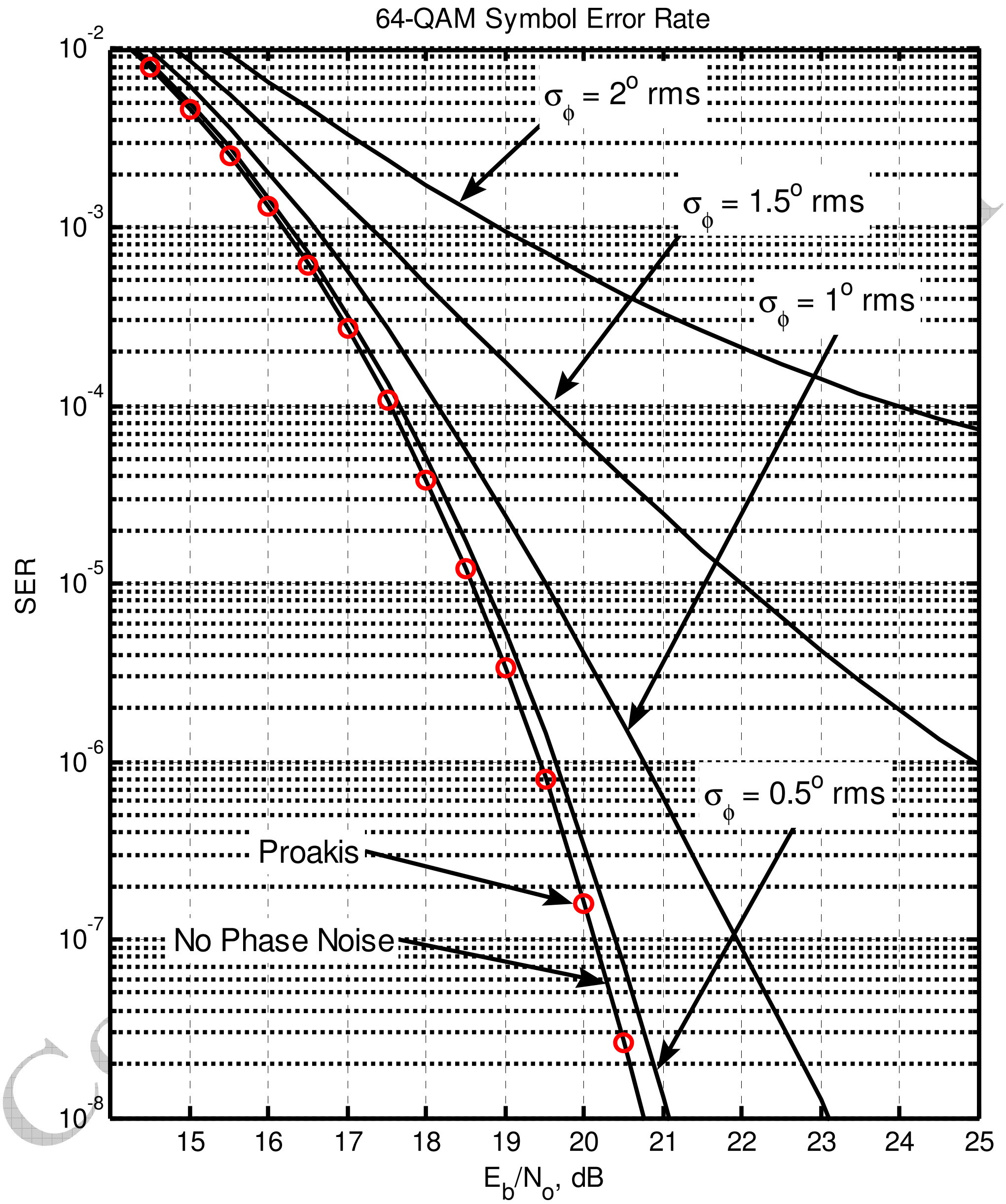

Figure 2-37 64-QAM uncoded symbol error rate with noisy local oscillator.[13] Circled datapoints are from (2.87).

---

[13] Book CD:\Ch5\u13159_qam_ser.m. See Section 5.5.3 for additional information. Circled datapoints are based on Proakis [3] page 282, equation (4.2.144), included in this text as (2.87).

A more detailed discussion of the Chernoff bound and its applications is available in [9].

Key Point: The Chernoff bound can be used to provide a tight upper-bound for the tail-probability of a one-sided probability density. It is a much tighter bound than the Chebyschev inequality given in Section 3.5. The bound given by (3.43) for the complementary error function can be helpful in bounding other performance measures.

3.7 CRAMER-RAO BOUND

The Cramer-Rao bound[16] (CRB) was first introduced in Section 1.4.4, and frequently appears in phase- and frequency-related estimation work when low SNR conditions prevail. Systems that asymptotically achieve the CRB are called *efficient* in estimation theory terminology. In this text, the CRB is used to quantify system performance limits pertaining to important quantities such as phase and frequency estimation, signal amplitude estimation, bit error rate, etc.

The CRB is used in Chapter 10 to assess the performance of several synchronization algorithms with respect to theory. Owing to the much larger signal SNRs involved with frequency synthesis, however, the CRB is rarely used in PLL-related synthesis work. The CRB is developed in considerable detail in the sections that follow because of its general importance, and its widespread applicability to the analysis of many communication system problems.

The CR bound provides a lower limit for the error covariance of any unbiased estimator of a deterministic parameter θ based on the probability density function of the data observations. The data observations are represented here by z_k for $k = 1, \ldots, N$, and the probability density of the observations is represented by $p(z_1, z_2, \ldots, z_N) = p(z)$. When θ represents a single parameter and θ-hat represents the estimate of the parameter based on the observed data z, the CRB is given by three equivalent forms as

$$\begin{aligned} \operatorname{var}\left[\left(\hat{\theta}-\theta\right)\right] &= \mathbf{E}\left[\left(\hat{\theta}-\theta\right)^2\right] \\ &\geq \left\{\mathbf{E}\left\{\left[\frac{\partial}{\partial\theta}\log_e p(\mathbf{z}\,|\,\theta)\right]^2\right\}\right\}^{-1} \\ &\geq -\left\{\mathbf{E}\left[\frac{\partial^2}{\partial\theta^2}\log_e p(\mathbf{z}\,|\,\theta)\right]\right\}^{-1} \\ &\geq \left\{\int_{-\infty}^{+\infty}\left[\frac{\partial}{\partial\theta}p(\mathbf{z})\right]^2\frac{1}{p(\mathbf{z})}d\mathbf{z}\right\}^{-1} \end{aligned} \tag{3.46}$$

The first form of the CR bound in (3.46) can be derived as follows. Since θ-hat is an unbiased (zero-mean) estimator of the deterministic parameter θ, it must be true that

$$\mathbf{E}\left(\tilde{\theta}\right) = \int_{-\infty}^{+\infty}\left[\hat{\theta}-\theta\right]p(\mathbf{z})d\mathbf{z} = 0 \tag{3.47}$$

in which $d\mathbf{z} = dz_1 dz_2 \ldots dz_N$. Differentiating (3.47) with respect to θ produces the equality

---

[16] See [10]–[14].

$$\operatorname{var}\left\{\hat{b}_o\right\} \geq \frac{\sigma^2}{M} \quad \text{for all cases} \tag{3.62}$$

$$\operatorname{var}\left\{\hat{\omega}_o T_s\right\} \geq \begin{cases} \dfrac{\sigma^2}{b_0^2 Q} & \text{Phase known, amplitude known or unknown} \\[2ex] \dfrac{12\sigma^2}{\mathrm{b}_0^2 M\left(M^2-1\right)} & \text{Phase unknown, amplitude known or unknown} \end{cases} \tag{3.63}$$

$$\operatorname{var}\left\{\hat{\theta}_o\right\} \geq \begin{cases} \dfrac{\sigma^2}{b_0^2 M} & \text{Frequency known, amplitude known or unknown} \\[2ex] \dfrac{12\sigma^2 Q}{b_0^2 M^2\left(M^2-1\right)} & \text{Frequency unknown, amplitude known or unknown} \end{cases} \tag{3.64}$$

In the formulation presented by (3.55), the signal-to-noise ratio ρ is given by $\rho = b_0^2 / (2\sigma^2)$.

For the present example, the CR bound is given by the top equation in (3.63) and is as shown in Figure 3-9 when the initial signal phase θ_o is known a priori. Usually, the carrier phase θ_o is not known a priori when estimating the signal frequency, however, and the additional unknown parameter causes the estimation error variance to be increased, making the variance asymptotically 4-times larger than when the phase is known a priori. This CR variance bound for this more typical unknown signal phase situation is shown in Figure 3-10.

Beginning with (3.57), a maximum-likelihood[17] frequency estimator can be formulated as described in Appendix 3A. It is insightful to compare this estimator's performance with its respective CR bound. For simplicity, the initial phase θ_o is assumed to be random but known a priori. The results for M = 80 are shown in Figure 3-11 where the onset of thresholding is apparent for $\rho \cong -2$ dB. Similar results are shown in Figure 3-12 for M = 160 where the threshold onset has been improved to about $\rho \cong -5$ dB.

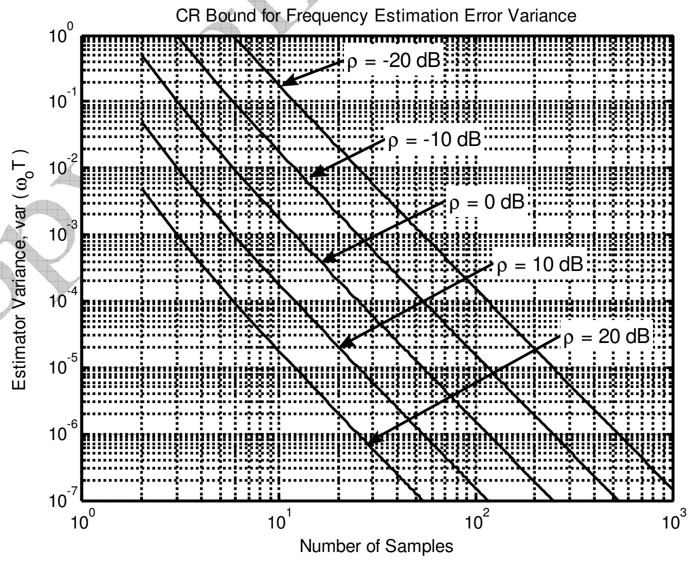

Figure 3-9 CR bound[18] for frequency estimation error with phase θ_o known a priori (3.63).

---

[17] See Section 1.4.2.

[18] Book CD:\Ch3\u13000_crb.m. Amplitude known or unknown, frequency unknown, initial phase known.

would be measured and displayed on a spectrum analyzer. Having recognized the carrier and continuous spectrum portions within (4.65), it is possible to equate[29]

$$\mathscr{L}(f) \cong P_\theta(f) \quad \text{rad}^2/\text{Hz} \tag{4.66}$$

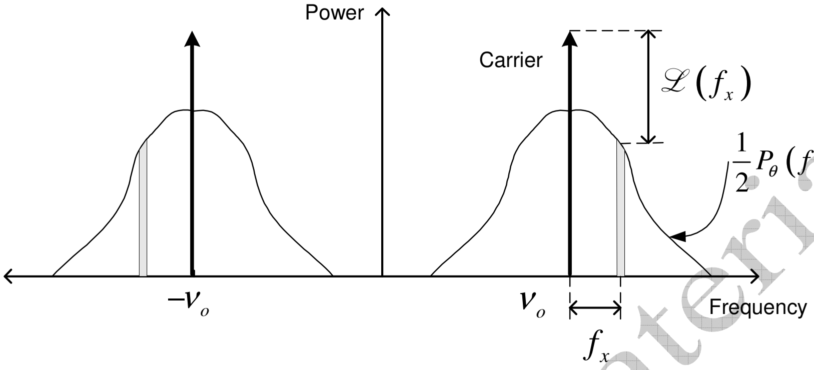

Figure 4-17 Resultant two-sided power spectral density from (4.65), and the single-sideband-to-carrier ratio $\mathscr{L}(f)$.

Both $\mathscr{L}(f)$ and $P_\theta(f)$ are *two-sided power spectral densities*, being defined for positive as well as negative frequencies.

The use of one-sided versus two-sided power spectral densities is a frequent point of confusion in the literature. Some PSDs are formally defined only as a one-sided density. Two-sided power spectral densities are used throughout this text (aside from the formal definitions for some quantities given in Section 4.6.1) because they naturally occur when the Wiener-Khintchine relationship is utilized.

4.6.1 Phase Noise Spectrum Terminology

A minimum amount of standardized terminology has been used thus far in this chapter to characterize phase noise quantities. In this section, several of the more important formal definitions that apply to phase noise are provided.

A number of papers have been published which discuss phase noise characterization fundamentals [34]–[40]. The updated recommendations of the IEEE are provided in [41] and those of the CCIR in [42]. A collection of excellent papers is also available in [43].

In the discussion that follows, the nominal carrier frequency is denoted by ν_o (Hz) and the frequency-offset from the carrier is denoted by f (Hz) which is sometimes also referred to as the *Fourier frequency*.

One of the most prevalent phase noise spectrum measures used within industry is $\mathscr{L}(f)$ which was encountered in the previous section. This important quantity is defined as [44]:

> $\mathscr{L}(f)$: The normalized frequency-domain representation of phase fluctuations. It is the ratio of the power spectral density in one phase modulation sideband, referred to the carrier frequency on a spectral density basis, to the total signal power, at a frequency offset f. The units[30] for this quantity are Hz^{-1}. The frequency range for f ranges from $-\nu_o$ to ∞. $\mathscr{L}(f)$ is therefore a two-sided spectral density and is also called *single-sideband phase noise*.

---

[29] It implicitly assumed that the units for $\mathscr{L}(f)$, dBc/Hz or rad^2/Hz, can be inferred from context.

[30] Also as rad^2/Hz.

$$z_i = p_i \exp\left(\frac{\alpha}{2}\Delta p\right) \tag{4B.10}$$

A minimum of one filter section per frequency decade is recommended for reasonable accuracy. A sample result using this method across four frequency decades using 3 and 5 filter sections is shown in Figure 4B-3.

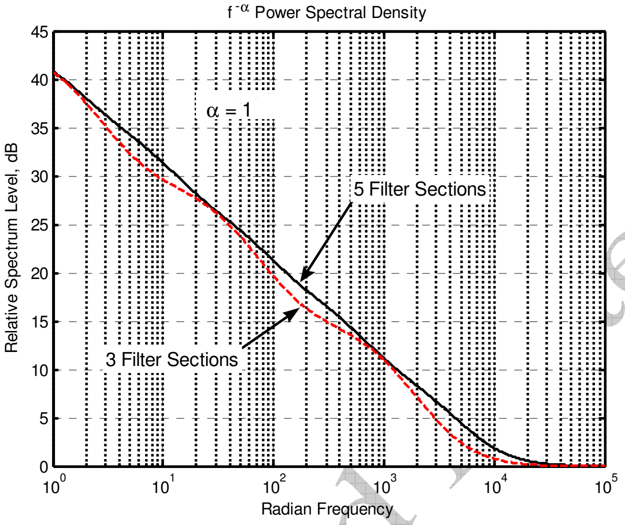

Figure 4B-3 $1/f$ noise creation using recursive $1/f^2$ filtering method[4] with white Gaussian noise.

$1/f^{\alpha}$ Noise Generation Using Fractional-Differencing Methods

Hosking [6] was the first to propose the *fractional differencing* method for generating $1/f^{\alpha}$ noise. As pointed out in [3], this approach resolves many of the problems associated with other generation methods. In the continuous-time-domain, the generation of $1/f^{\alpha}$ noise processes involves the application of a nonrealizable filter to a white Gaussian noise source having $s^{-\alpha/2}$ for its transfer function. Since the z-transform equivalent of $1/s$ is $H(z) = (1 - z^{-1})^{-1}$, the *fractional digital filter* of interest here is given by

$$H_{\alpha}(z) = \frac{1}{\left(1 - z^{-1}\right)^{\alpha/2}} \tag{4B.11}$$

A straightforward power series expansion of the denominator can be used to express the filter as an infinite IIR filter response that uses only integer-powers of z as

$$H_{\alpha}(z) \approx \left[1 - \frac{\alpha}{2}z^{-1} - \frac{\frac{\alpha}{2}\left(1 - \frac{\alpha}{2}\right)}{2!}z^{-2} - \ \ldots\right]^{-1} \tag{4B.12}$$

in which the general recursion formula for the polynomial coefficients is given by

---

[4] Book CD:\Ch4\u13070_recursive_flicker_noise.m.

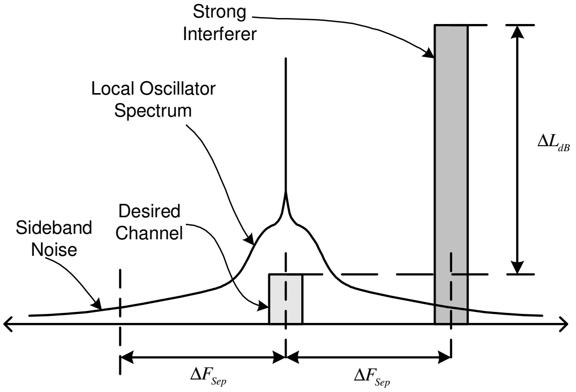

Figure 5-9 Strong interfering channels are heterodyned on top of the desired receive channel by local oscillator sideband noise.

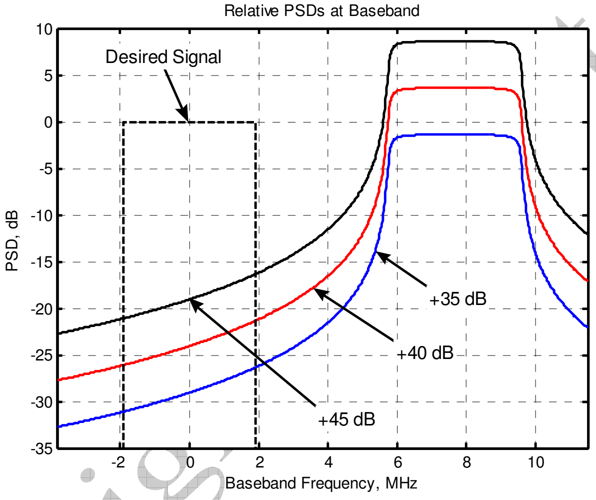

Figure 5-10 Baseband spectra[10] caused by reciprocal mixing between a strong interferer that is offset 4*B* Hz higher in frequency than the desired signal and stronger than the desired signal by the dB amounts shown.

The first term in (5.28) $2BL_{Floor}$ is attributable to the ultimate blocking performance of the receiver as discussed in Section 5.3. The resultant output SNR versus input SNR is given by

$$SNR_{out} = \left[\frac{1}{SNR_{in}} + \frac{\sigma^2_{MFX}}{2BL_{IQ}}\right]^{-1} \tag{5.29}$$

It is worthwhile to note that the interfering spectra in Figure 5-10 are not uniform across the matched-filter frequency region [–*B*, *B*]. Multicarrier modulation like OFDM (see Section 5.6) will potentially be affected differently than single-carrier modulation such as QAM (see Section 5.5.3) when the interference spectrum is not uniform with respect to frequency.

The result given by (5.29) is shown for several interfering levels versus receiver input SNR in Figure 5-11.

---

[10] Book CD:\Ch5\u13157_rx_desense.m. Lorentzian spectrum parameters: $L_o = -90$ dBc/Hz, $f_c = 75$ kHz, $L_{Floor} = -160$ dBc/Hz, $B = 3.84/2$ MHz.

of 3° rms phase noise is shown in Figure 5B-8. The tail probability is worse than the exact computations shown in Figure 5-17 but the two results otherwise match very well.

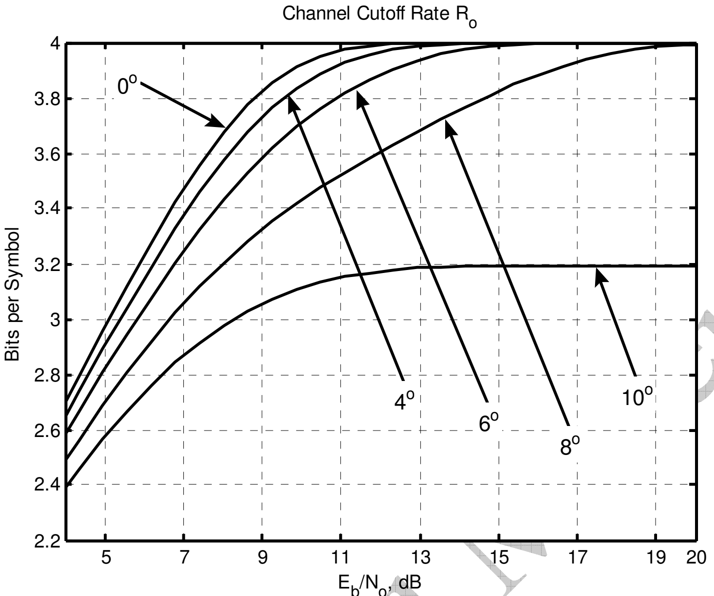

Figure 5B-6 Channel cutoff rate,[7] R_o, for 16-QAM with static phase errors as shown, from (5B.16).

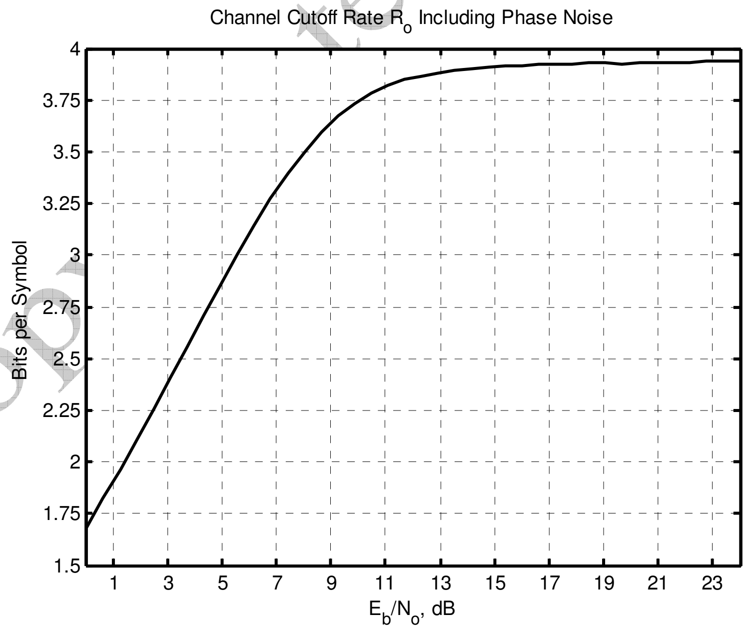

Figure 5B-7 R_o for[8] 16-QAM versus E_b/N_o for 5° rms phase noise from (5B.18) (to accentuate loss in R_o even at high SNR values).

---

[7] Book CD:\Ch5\u13176_rolo.m.

[8] Ibid.

required, however, because the offset current will introduce its own shot-current noise contribution, and the increased duty-cycle of the charge-pump activity will also introduce additional noise and potentially higher reference spurs. Single-bit Δ-Σ modulators are attractive in this respect because they lead to the minimum-width phase-error distribution possible.

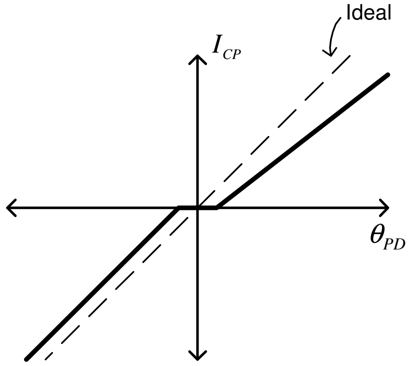

Figure 8-70 Charge-pump (i) dead-zone and (ii) unequal positive versus negative error gain.

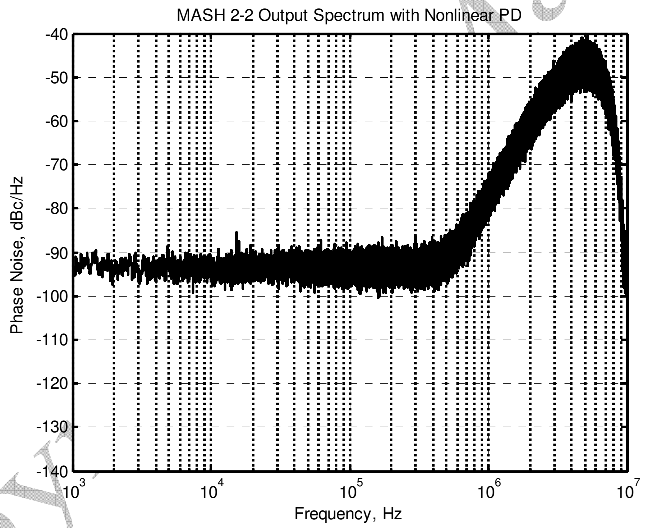

Figure 8-71 Phase error power spectral density[48] for the MASH 2-2 Δ-Σ modulator shown in Figure 8-55 with $M = 2^{22}$, $P = M/2 + 3{,}201$, and 2% charge-pump gain imbalance. Increased noise floor and discrete spurs are clearly apparent compared to Figure 8-56.

Classical random processes theory can be used to provide several useful insights about nonlinear phase detector operation. In the case of unequal positive-error versus negative-error phase detector gain, the memoryless nonlinearity can be modeled as

$$\theta_{pd} = \phi_{in} + \alpha\left(\phi_{in} > 0\right)\phi_{in} \tag{8.39}$$

where α represents the additional gain that is present for positive phase errors. The instantaneous phase error due to the modulator's internal quantization creates a random phase error sequence that can be represented by

---

[48] Book CD:\Ch8\u12735_MASH2_2_nonlinear.m.

the sampling-point within each symbol-period after the datalink signal has been fully acquired. In the example results that follow, the data source is assumed to be operating at 1 bit-per-second, utilizing square-root raised-cosine pulse-shaping with an excess bandwidth parameter $\beta = 0.50$ at the transmitter. The eye-diagram of the signal at the transmit end is shown in Figure 10-15. The ideal matched-filter function in the CDR is closely approximated by an $N = 3$ Butterworth lowpass filter having a –3 dB corner frequency of 0.50 Hz like the filter used in Section 10.4. The resulting eye-diagram at the matched-filter output is shown in Figure 10-16 for $E_b/N_o = 25$ dB.

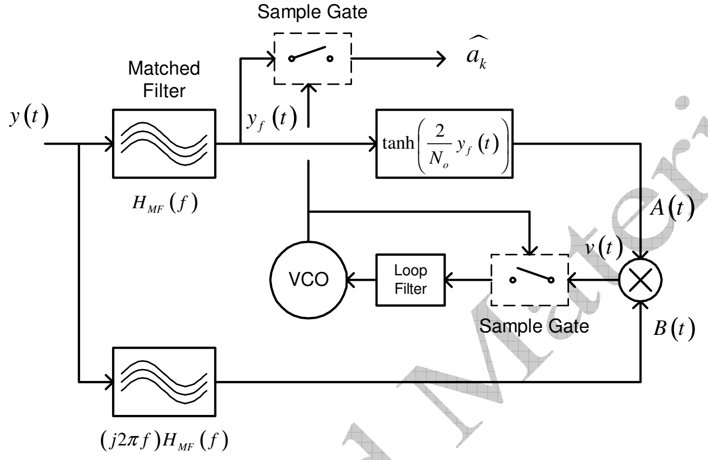

Figure 10-14 ML-CDR implemented with continuous-time filters based on the timing-error metric given by (10.21).

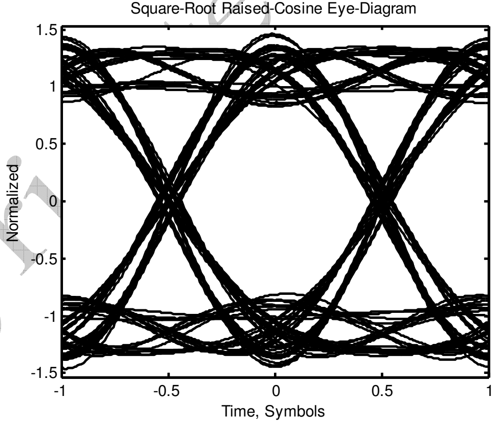

Figure 10-15 Eye diagram[15] at the data source output assuming square-root raised-cosine pulse shaping with an excess bandwidth parameter $\beta = 0.50$.

A clear understanding of the error metric represented by $v(t)$ in Figure 10-14 is vital for understanding how the CDR operates. The metric is best described by its *S-curve* behavior versus input E_b/N_o as shown in Figure 10-17. Each curve is created by setting the noise power spectral density N_o for a specified E_b/N_o value with $E_b = 1$, and computing the average of $v(kT_{sym} + \varepsilon)$ for $k = [0, K]$ as the timing-error ε is swept across $[0, T_{sym}]$. The slope of each S-curve near the zero-error steady-state tracking value determines the linear gain of the metric that is needed to compute the closed-loop bandwidth, loop stability margin, and other important quantities. For a given input SNR,

---

[15] Book CD:\Ch10\u14004_ml_cdr.m.

the corresponding S-curve has only one timing-error value ε_o for which the error metric value is zero and the S-curve slope has the correct polarity. As the gain value changes with input E_b/N_o, the closed-loop parameters will also vary. For large gain variations, the Haggai loop concept explored in Section 6.7 may prove advantageous.

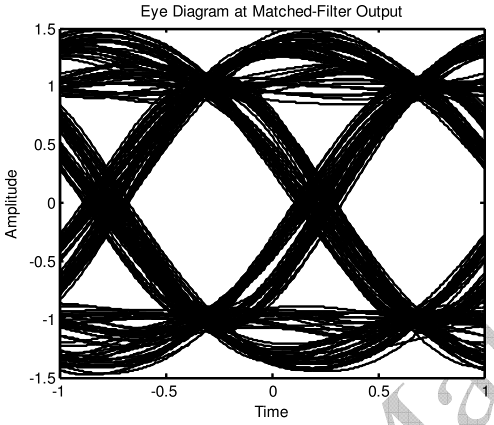

Figure 10-16 Eye diagram[16] at the CDR matched-filter output for $E_b/N_o = 25$ dB corresponding to the data source shown in Figure 10-15 and using an $N = 3$ Butterworth lowpass filter with $BT = 0.50$ for the approximate matched-filter.

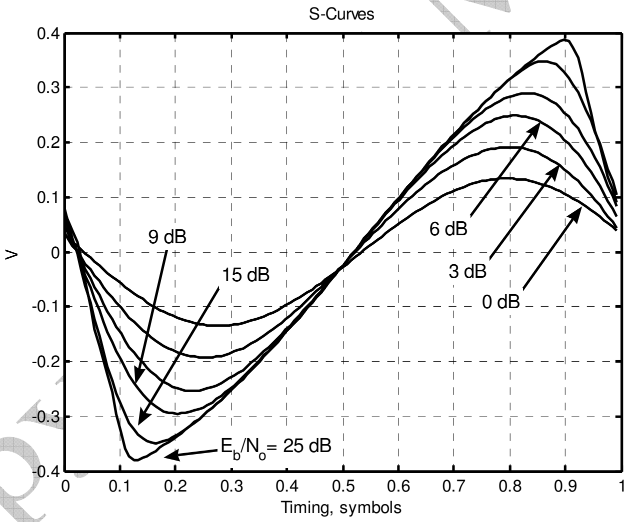

Figure 10-17 S-curves[17] versus E_b/N_o corresponding to Figure 10-16 and ideal ML-CDR shown in Figure 10-14. $E_b = 1$ is assumed constant.

A second important characteristic of the timing-error metric is its variance versus input E_b/N_o and static timing-error ε. For this present example, this information is shown in Figure 10-18. The variance understandably decreases as the input SNR is increased, and as the optimum time-alignment within each data symbol is approached. The variance of the recovered data clock σ_{clk}^2 can be closely estimated in terms of the tracking-point voltage-error variance from Figure 10-18 denoted by σ_{ve}^2 (V^2), the slope (i.e., gain) of the corresponding S-curve (K_{te}, V/UI) from Figure 10-17, the symbol rate F_{sym} ($= 1/T_{sym}$), and the one-sided closed-loop PLL bandwidth B_L (Hz) as

---

[16] Ibid.

[17] Ibid.